New solid electrolyte $Na_9Al(MoO_4)_6$: structure and Na^+ ion conductivity

Article

New Solid Electrolyte Na9Al(MoO4)6: Structure and Na+ Ion Conductivity

Aleksandra A. Savina, Vladimir A. Morozov, Anton L. Buzlukov, Irina Yu. Arapova, Sergey Yu. Stefanovich, Yana V. Baklanova, Tatiana A. Denisova, Nadezhda I. Medvedeva, Michel Bardet, Joke Hadermann, Bogdan I. Lazoryak, and Elena G. Khaikina

Chem. Mater., **Just Accepted Manuscript** • Publication Date (Web): 26 Sep 2017

New Solid Electrolyte $Na_9Al(MoO_4)_6$: Structure and Na^+ Ion Conductivity

Aleksandra A. Savina,[*,†] Vladimir A. Morozov,[‡] Anton L. Buzlukov,[§] Irina Yu. Arapova,[§] Sergey Yu. Stefanovich,[‡] Yana V. Baklanova,[††] Tatiana A. Denisova,[††] Nadezhda I. Medvedeva,[††] Michel Bardet,[‡,§§], Joke Hadermann,[†††] Bogdan I. Lazoryak,[‡] Elena G. Khaikina[†,‡‡‡]

[†] *Baikal Institute of Nature Management, Siberian Branch, Russian Academy of Sciences, Sakh'yanova St. 6, Ulan-Ude, 670047 Buryat Republic, Russia*

[‡] *Department of Chemistry, Moscow State University, 119899, Moscow, Russia*

[§] *Institute of Metal Physics, Ural Branch, Russian Academy of Science, S. Kovalevskaya St. 18, 620137 Ekaterinburg, Russia*

[††] *Institute of Solid State Chemistry, Ural Branch, Russian Academy of Science, Pervomayskaya St. 91, 620990 Ekaterinburg, Russia*

[‡‡] *Universite Grenoble Alpes, INAC, MEM/LRM, F-38000 Grenoble, France*

[§§] *CEA, INAC, MEM/LRM, F-38054 Grenoble, France*

[†††] *EMAT, University of Antwerp, Groenenborgerlaan 171, Belgium B-2020*

[‡‡‡] *Buryat State University, Smolin St. 24a, Ulan-Ude, 670000 Buryat Republic, Russia*

[*]Corresponding author: Aleksandra A. Savina

Tel.: +7(301) 2434753

Fax.: +7(301) 2434753

E-mail: Alex551112@mail.ru

Address: Baikal Institute of Nature Management, Siberian Branch, Russian Academy of Sciences, Sakh'yanova St. 6, Ulan-Ude, 670047, Buryat Republic, Russia.

ABSTRACT: Solid electrolytes are important materials with a wide range of technological applications. This work reports the crystal structure and electrical properties of a new solid electrolyte $Na_9Al(MoO_4)_6$. The monoclinic $Na_9Al(MoO_4)_6$ consists of isolated polyhedral $[Al(MoO_4)_6]^{9-}$ clusters composed of a central AlO_6 octahedron sharing vertices with six MoO_4 tetrahedra to form a 3D framework. The AlO_6 octahedron also shares edges with one $Na1O_6$-octahedron and two $Na2O_6$-octahedra. Na3–Na5 atoms are located in the framework cavities. The structure is related to that of the sodium ion conductor II-$Na_3Fe_2(AsO_4)_3$. High temperature conductivity measurements revealed that the conductivity of $Na_9Al(MoO_4)_6$ at T = 803 K equals $\sigma = 1.63 \cdot 10^{-2}$ S·cm^{-1}. The temperature behavior of the ^{23}Na and ^{27}Al NMR spectra and the spin-lattice relaxation rates of the ^{23}Na nuclei indicate the presence of fast Na^+ ion diffusion in the studied compound. At T < 490 K, diffusion occurs by means of Na^+ ion jumps exclusively through the sublattice of Na3–Na5 positions, whereas the Na1–Na2 become involved in the diffusion processes (through the chemical exchange with the Na3–Na5 sublattice) only at higher temperatures.

1. INTRODUCTION

Solid materials with electrical conductivity from ~10^{-3} to 10^{-1} S/cm (comparable with liquid electrolytes) are termed as "solid electrolytes" or "superionic solids". Superionic solids have been widely investigated in view of their unique transport properties and applications. [1–4] These applications include gas sensors for carbon dioxide[2], anodes and cathodes in Li- or Na-ion batteries[3,5], fuel cells[5] and solid state power sources for medical devices.[6] $Na_{2.67}Mn_{1.67}(MoO_4)_3$ with the alluaudite[7] related structure can effectively cycle Na^+ ions reversibly at room temperature, and has a high average voltage (3.45 V), high capacity and good cyclability for rechargeable Na-ion battery applications.[8]

In addition to the use in Na-ion batteries, double molybdates containing both alkali and trivalent cations are attractive for many industrial applications, including solid electrolytes, ferroelectrics, photocatalysts and optical materials (white-light-emitting diodes and solid state lasers).[9–35] The $Na_xR_y(MoO_4)_{(x+3y)/2}$ (R – trivalent cations) molybdates found in the Na_2MoO_4–$R_2(MoO_4)_3$ systems are known to exist in a wide range of x:y ratios. The vast majority of the published $Na_xR_y(MoO_4)_{(x+3y)/2}$ (R – trivalent cations) molybdates exhibits the ratio Na:R=x/y=1:1 nevertheless there are also compounds with Na:R compositions 5:1, 1:5, 3:1 and 9:1.[9, 10]

The first synthesis and determination of the unit cell parameters of the $Na_9R(MoO_4)_6$ (R = In, Sc) compounds was done by *Velikodny*[36]. Later, the structures of $Na_9Fe(MoO_4)_6$[35] and $Na_9Sc(MoO_4)_6$[37] were solved in the space group $R\bar{3}$ from single crystal diffraction and X-ray powder diffraction data, respectively. The basic structure units of $Na_9R(MoO_4)_6$ (R = Fe, Sc) and low-temperature trigonal α-$Na_9Cr(MoO_4)_6$ (sp. gr. $R\bar{3}c$)[38] are isolated polyhedral $[R(MoO_4)_6]^{9-}$ clusters composed of a central RO_6 octahedron sharing vertices with six MoO_4 tetrahedra to form an open framework in which the Na^+ cations are bound to the free vertices of the MoO_4 tetrahedra. In comparison with $Na_9R(MoO_4)_6$ (R = Fe, Sc, Cr), the alluaudite[7] related structure of monoclinic high temperature β–$Na_9Cr(MoO_4)_6$ (space group $C2/c$) is constituted of infinite layers formed by links between M_2O_{10} (M = Cr/Na) dimers and MoO_4 tetrahedra.[39] Earlier high Na^+ ion conductivity was found in $Na_9Fe(MoO_4)_6$[33]. However, the mechanism of ion transport was not determined.

The present work reports the synthesis and characterisation of a new $Na_9Al(MoO_4)_6$ molybdate by X-ray powder diffraction (PXRD) and transmission electron microscopy (TEM). Ion conductivity properties were studied by impedance spectroscopy and the diffusion processes of ions were investigated by Nuclear Magnetic Resonance (NMR) spectroscopy. It should be noted that $Na_9Al(MoO_4)_6$ is more convenient for NMR studies than $Na_9Fe(MoO_4)_6$. The presence of the ^{27}Al nucleus provides an additional channel for obtaining information, whereas the paramagnetic Fe^{3+} ions can lead to the appearance of substantial hyperfine interactions between

the nuclear and electronic subsystems, which considerably complicates or even makes impossible the interpretation of NMR results (in the sense of ionic dynamics studies).

2. EXPERIMENTAL SECTION

2.1. Materials and Sample Preparation. $Na_9Al(MoO_4)_6$ was synthesized by annealing stoichiometric mixtures of Na_2MoO_4 and $Al_2(MoO_4)_3$ at 773–803 K for 100–140 h with intermittent grinding every 15 h and slow cooling in the furnace from 773–803 K to room temperature (RT). PXRD patterns of the prepared compound do not contain reflections of parent or foreign phases. The final powder product was of white color. $Na_9Al(MoO_4)_6$ was found to melt at 873.5±0.2 K and Na_2MoO_4, $Na_2Mo_2O_7$ and $NaAl(MoO_4)_2$ along with the parent phase $Na_9Al(MoO_4)_6$ were found in the solidified melt. A stoichiometric mixture of $Al(NO_3)_3{\cdot}9H_2O$ (analytical grade) and MoO_3 (reagent grade) was used for the synthesis of $Al_2(MoO_4)_3$ at 573–723 K for 25–40 h followed by annealing at 873 K for 60 h. Anhydrous Na_2MoO_4 was obtained by calcination of the corresponding crystalline hydrate at 823–873 K. PXRD patterns of the prepared $Al_2(MoO_4)_3$ and Na_2MoO_4 have been checked by using JCPDS PDF-2 Data Base and do not contain reflections of initial phases.

2.2. Characterization. PXRD patterns were performed with a D8 ADVANCE Bruker diffractometer (Cu*K*α radiation, λ = 1.5418 Å, reflection geometry). PXRD data were collected at RT over the 7°–100° 2θ range with steps of 0.02076°. Le Bail decomposition to determine the lattice parameters[40] and the Rietveld analysis were performed using the JANA2006 software.[41] Illustrations were produced with this package in combination with the program VESTA.[42]

Thermoanalytic studies were carried out on a STA 449 F1 Jupiter NETZSCH thermoanalyser (Pt crucible, heating rate of 10 degree/min in Ar stream).

Determination of chemical composition was carried out by X-ray fluorescence spectroscopy (XRFs) on a PANanalytical Axios Advanced spectrometer. Characteristic X-rays were excited using a 4 kW Rh-anode X-ray tube. The excited radiation was recorded by a scanning channel with five exchangeable wave crystals and a detector. Measurements were made in transmission geometry in vacuum. Specimens were prepared as pellets with a binder (C_8H_9) in proportion 5:1.

The second-harmonic generation (SHG) response of the powder samples was measured in a reflection mode. A Q-switch pulsed Nd:YAG Minilite-I laser operating at λ_ω = 1064 nm was used as the radiation source (repetition frequency 15 Hz, repetition rate of 4 impulses/s, pulse duration 3 ns). The experimental set-up was described elsewhere.[43] The optical nonlinearity of the materials was evaluated relative to an α-quartz reference (polycrystalline α-SiO_2 with 3–5 μm particles size), $I_{2\omega}/I_{2\omega}(SiO_2)$. In fine powders, $I_{2\omega}/I_{2\omega}(SiO_2)$ is a quadratic function of spatially

averaged components of the optical nonlinearity tensor.[44] The incident beam peak power was about 0.1 MW on a spot of 3-mm diameter on the surface of the sample.

Selected area electron diffraction (SAED) patterns of $Na_9Al(MoO_4)_6$ at RT were obtained using a Philips CM20 transmission electron microscope equipped with a LINK-2000 EDX attachment. Samples for TEM were prepared by crushing powders in agate mortars and dispersing them in methanol. After treatment in an ultrasonic bath to disperse crystallites, a few drops of the dispersion were placed on copper grids with a holey carbon film.

Ceramic disks for dielectric investigations were prepared by pressing of powders at 1 kbar and sintering at 843 K for 4 h. The densities of the resultant pellets were typically 90–95 % of theoretical ones. The disks were 7–8 mm in diameter and 1–2 mm thick, they were electroded by painting of colloid platinum on their large surfaces with subsequent one hour annealing at about 823 K. The direct current (DC) electrical conductivity was qualitatively controlled with a B7-38 microamperemeter. Electrical conductivity of the samples was determined by impedance spectroscopy in the temperature range 343–823 K at heating and cooling rates of 2 K/min using two-probe measurements in NorECs ProboStat cell. The signal was monitored with a Novocontrol Beta-N impedance analyzer at applied voltage of 0.5 V at selected frequencies in 0.3 Hz–1 MHz interval.

The static NMR experiments were performed over the temperature range 300–750 K. The experimental data were obtained on an AVANCE III 500WB BRUKER spectrometer in an external magnetic field 11.74 T. A commercial high-temperature wide-line probe (Bruker Biospin GmbH), including a Pt-wired rf coil, nonmagnetic heater, and the type-E thermocouple, was used to heat a sample in static air atmosphere. The sample was tightly packed inside an open quartz ampule throughout NMR measurements. The static spectra for ^{23}Na (the Larmor frequency $^{23}\omega_0/2\pi$ = 132.29 MHz, the nuclear spin ^{23}I = 3/2, quadrupole moment ^{23}Q = 0.108 barn) and for ^{27}Al ($^{27}\omega_0/2\pi$ = 130.32 MHz, ^{27}I = 5/2, ^{27}Q = 0.150 barn) were acquired by Fourier transform of both free induction decay: τ–*acq*, and (in some cases) spin echo signals: τ–t_{del}–2τ–t_{del}–*acq*. The duration of the exciting pulse was, τ = 2 μs, which corresponds to the nuclear magnetization tip angle, $\theta \sim 60°$. The spin-lattice relaxation times for ^{23}Na nuclei were measured by the "inversion-recovery" technique: 2τ–t_{del}–τ–*acq*.

The MAS NMR spectra were obtained with RT bearing gas by using the standard Bruker MAS NMR probeheads with 1.3 mm (on an AVANCE DSX 200 NMR spectrometer in an external magnetic field 4.7 T), and 3.2 mm rotors (AVANCE III 500WB spectrometer, 11.7 T), and standard Agilent 4.0 mm MAS Probehead (AGILENT VNMR 400WB spectrometer, 9.4 T). As for the static regime, the ^{23}Na MAS NMR spectra were acquired by Fourier transform of free

induction decay and/or spin echo signals with the exciting pulse 2 μs. In all cases the spectra deconvolution was performed by using the DMFit program.[45]

In order to provide a reliable assignment of the ^{23}Na NMR resonances to the nonequivalent Na positions, the quadrupole interaction parameters were evaluated within the density functional theory (DFT). The calculations were performed using the projector-augmented wave (PAW) method as implemented in the Vienna *ab initio* simulation package (VASP)[46–48] and the Perdew–Burke-Ernzerhof (PBE)[48] generalized-gradient approximation (GGA) for potentials. Plane-wave cutoff energy was set to 400 eV for all calculations with convergence criterion for the total energy of 0.01 meV. For the Brillouin-zone sampling, we used the Monkhorst-Pack scheme[49] with a mesh of 6×6×6 irreducible *k*-points. The initial structural data for *ab initio* calculations were taken from experiment and then the structure was relaxed with respect to atomic positions via a conjugate gradient algorithm until the forces on all unconstrained atoms were less than 0.005 eV/Å. The electric field gradient (EFG) tensor is calculated directly from the non-spherical part of the potential and its diagonalization provides the eigenvalues V_{xx}, V_{yy} and V_{zz}. If $|V_{zz}| > |V_{yy}| > |V_{xx}|$, the largest principal axis component V_{zz} determines the quadrupole frequency $\nu_Q = 3eQV_{zz}/2I(2I-1)h$, and the asymmetry parameter $\eta = (V_{yy} - V_{xx})/V_{zz}$.

3. Results and Discussion

3.1. Elemental Composition and SHG study. The determination of chemical composition of the polycrystalline $Na_9Al(MoO_4)_6$ performed by XRFs gave for the Na, Al and Mo content in the sample: 17.4:2.4:48.1 wt.% (calculated: 17.34:2.26:48.23 wt.%). SHG study revealed an insignificant value of SHG responses (<0.1) for $Na_9Al(MoO_4)_6$ and indicated a centrosymmetric space group for the structure.

3.2. Preliminary PXRD characterization and validating the refinement model. The determination of $Na_9Al(MoO_4)_6$ unit cell parameters from PXRD patterns using Le Bail decomposition revealed that all reflections could be indexed assuming $Na_9Al(MoO_4)_6$ is isostructural to $Na_9Fe(MoO_4)_6$[35] (space group $R\bar{3}$: a = 14.64268(8) Å, c = 19.3129(1) Å; values of structural *R*-factors: R_P = 3.65 % and R_{wP} = 5.09 %). On the other hand, similar results were obtained using the model of α-$Na_9Cr(MoO_4)_6$[38] (sp. gr. $R\bar{3}c$: a = 14.64268(5) Å, c = 19.3128(1) Å; values of structural *R*-factors: R_P = 3.66 % and R_{wP} = 5.11 %). The difference between the $R\bar{3}$ and $R\bar{3}c$ space groups can be made using the fact that the 000*l*: l=2n+1 reflections are forbidden by the $R\bar{3}c$ symmetry. PXRD patterns of $Na_9Al(MoO_4)_6$ over a small 2θ range around the 0003 and 0009 reflections are shown in Figure 1. The 0003 and 0009 (*hkil*) reflections are not present on the PXRD patterns, supporting the choice of the space group $R\bar{3}c$. However, several extra

reflections with small intensity were visible in the PXRD pattern, which could not be assigned to any previously known phase.

Nevertheless, the $Na_9Al(MoO_4)_6$ crystal structure was refined according to the Rietveld method[50] in both the $R\bar{3}$ and $R\bar{3}c$ models starting with the atomic coordinates of the $Na_9Fe(MoO_4)_6$[35] and α-$Na_9Cr(MoO_4)_6$[38] structures. Details of the $Na_9Al(MoO_4)_6$ structure refinement are summarized in Table 1. Atomic coordinates, equivalent isotropic displacement parameters and bond lengths are listed in Tables S1 and S2 of the Supporting information. As can be deduced from Table 1, the $R\bar{3}$ model is characterized by essentially lower values of structural *R*-factors and max./min. residual density peaks but with large numbers of refined parameters. However, the refinement of the $R\bar{3}c$ model results in large atomic displacement parameters for Na in the Na1 and Na2 positions ($U_{iso.}$ = 0.051(3) and $U_{iso.}$ = 0.036(2), respectively) and O1–O3 oxygen atoms ($U_{iso.}$ = 0.031(3)–0.038(3)) (Table S2 of the Supporting information).

So despite the fact that 0003 and 0009 reflections are absent from the $Na_9Al(MoO_4)_6$ PXRD patterns, the refinement in the $R\bar{3}$ model gives better results. Therefore, we will clarify the correct space group using SAED.

3.3. SAED Study. The detailed analysis of the SAED patterns revealed that the real structure of $Na_9Al(MoO_4)_6$ requires a monoclinic distortion of the rhombohedral sublattice and has a *Cc* or *C2/c* space group. The insignificant value of SHG responses (<0.1) for $Na_9Al(MoO_4)_6$ indicated a centrosymmetric *C2/c* space group for the structure. The ED patterns along the main zone axes for $Na_9Al(MoO_4)_3$ are shown in Figure 2. The relation between the unit cell vectors of the rhombohedral (*R* refers to the $R\bar{3}c$ unit cell) and the monoclinic unit cell is as follows: $[0001]_R = [101]$, $[\bar{1}101]_R = [001]$, $[\bar{1}10\bar{2}]_R = [100]$ and $[11\bar{2}0]_R = [010]$. The difference between the experimental (assigned as monoclinic) ED pattern and a rhombohedral pattern is the deviation from 90° of the angle between the $\bar{2}02$ and 402 vectors (angle is ~88°) occurring in the [010] ED pattern. In the case of a rhombohedral $R\bar{3}c$ lattice, the angle between the corresponding $000l_R$ and the $\bar{h}\,h00_R$ rows in the $[11\bar{2}0]_R$ pattern should be equal to 90°.

The ED patterns can be completely indexed in the *C2/c* space group with unit cell parameters: *a* = 15.37 Å, *b* = 14.62 Å, *c* = 10.60 Å and β = 94°. The reflections on the [001] ED pattern obey the extinction conditions *hk*0: $h + k = 2n$ indicating the *C*-centered unit cell. The [100] ED pattern exhibits 00*l*:$l = 2n+1$ reflections forbidden by the *C*2/*c* symmetry. Upon tilting the sample around the 00*l* reciprocal lattice row the reflections with 00*l*:$l = 2n+1$ weaken and finally vanish. Therefore, the appearance of these forbidden reflections is attributed to multiple diffraction. The 00*l*:$l = 2n+1$ reflections are absent in the $[010]^*$ zone where the conditions for their appearance due to multiple diffraction are not fulfilled.

3.4. Refinement of crystal structure. On the basis of the ED data, the crystal structure of $Na_9Al(MoO_4)_6$ was finally refined in the monoclinic *C*2/*c* space group with unit cell parameters *a* = 15.4067(3), *b* = 14.6428(3), *c* = 10.6250(2) Å, *β* = 93.991(2)°. The structural data for the α-$Na_9Cr(MoO_4)_6$ structure[38] were used for the refinement. The relation between the monoclinic *C*2/*c* cell and the trigonal $R\bar{3}c$ subcell is shown in Figure 3. The atom coordinates for the *C*2/*c* model of the $Na_9Al(MoO_4)_6$ structure have been obtained by transforming the coordinates of the corresponding positions in the *α*-$Na_9Cr(MoO_4)_6$ substructure in accordance with the transformation matrix.[1]

Details of the $Na_9Al(MoO_4)_6$ structure refinement are summarized in Table 1, and atomic coordinates, equivalent isotropic displacement parameters and bond lengths are listed in Tables S1 and S2 of the Supporting information. The calculated and residual PXRD patterns are shown in Figure 4. Table 1 shows that the *C*2/*c* model has essentially lower structural *R*-factors and max./min. residual density peaks than the other refined models.

3.5. Specific features of $Na_9Al(MoO_4)_6$ crystal structures. Similar to $Na_9R(MoO_4)_6$ (*R* = Fe[35], Sc[37]) and the low-temperature *α*-$Na_9Cr(MoO_4)_6$ phase[38], the basic structure units of $Na_9Al(MoO_4)_6$ are isolated polyhedral $[Al(MoO_4)_6]^{9-}$ clusters, composed of a central AlO_6 octahedron sharing vertices with six MoO_4 tetrahedra to form a 3D framework. Figure 5 illustrates a projection of the $Na_9Al(MoO_4)_6$ structure and a view of the $Na_9Fe(MoO_4)_6$ structure showing only the $[Fe(MoO_4)_6]^{9-}$ clusters. In the $Na_9Al(MoO_4)_6$ structure, the central AlO_6-octahedron of the $[Al(MoO_4)_6]^{9-}$ cluster (Figure 6*a*) shares edges with one $Na1O_6$-octahedron and two $Na2O_6$-octahedra (Figure 6*b*). Na3–Na5 atoms are located in the framework cavities.

In the structure, all molybdenum atoms have the usual tetrahedral coordination with distances Mo–O 1.70(4)–1.93(3) Å, the Al^{3+} cations are octahedrally coordinated with bond lengths Al–O 1.83(4)–2.02(6) Å (Table S2 of the Supporting information). The Na^+ cations occupy five sites (Na1–Na5) with different O-environments. The monoclinic distortion of the rhombohedral $R\bar{3}c$ sublattice and the rotation of the MoO_4 tetrahedra lead to a distortion of the Na polyhedra in comparison with the $Na_9R(MoO_4)_6$ (*R* = Fe[35], Sc[37], *α*-Cr[38]) structures. Cations Na1–Na2 and Na4–Na5 are located in a strongly distorted octahedral environment [$d_{Na1—O}$ = 2.27(6)–2.51(5) Å; $d_{Na2–O}$ = 2.28(5)–2.83(5) Å; $d_{Na4–O}$ = 2.21(5)–2.85(5) Å; $d_{Na5–O}$ = 2.26(6)–

[1] The transformation matrix from the $R\bar{3}c$ subcell (s) to the monoclinic supercell (*C*2/*c*) is $T = \begin{pmatrix} 1/3 & -1/3 & 2/3 \\ 1 & 1 & 0 \\ -1/3 & 1/3 & 1/3 \end{pmatrix}$ in the matrix equation $A_{C2/c} = A_s * T$.

2.73(5) Å]. The lowest distortion of the polyhedron is observed for the Na1 position and the difference between shorter (Na1–O4) and long distances (Na1–O3) is 10.6%.

Similar differences in $Na2O_6$, $Na4O_6$ and $Na5O_6$ polyhedra are much larger (24.1%, 29.0% and 20.8%, respectively). The type of the polyhedron for the Na3 position cannot be clearly defined. Four Na3–O distances (d_{Na3-O} = 2.15(3)–2.72(5) Å) are significantly shorter than two distances between Na3 and two other (O5 and O7) oxygen atoms (d_{Na3-O5} = 3.01(5) Å and d_{Na3-O7} = 2.89(4) Å) (Table S2 of the Supporting information). The differences between the short (Na3–O2) and long distances (Na3–O7 and Na3–O5) in the $Na3O_6$ polyhedron are 34.4 and 40%, respectively.

The structural organization of $Na_9R(MoO_4)_6$ is close to that of the well-known sodium ion conductor II-$Na_3Fe_2(AsO_4)_3$ (sp. gr. $R\bar{3}c$, Z = 12)[51]. The structural family of II-$Na_3Fe_2(AsO_4)_3$ also involves II-$Na_3M_2(AsO_4)_3$ (M = Al, Ga, Cr),[51, 52] $Na_7Fe_4(AsO_4)_6$,[53] $Na_3Fe_2(PO_4)_3$,[54] and $Na_7Fe_4(PO_4)_6$.[55] Note that a decrease of symmetry to monoclinic (space group. $C2$) has previously also been observed in α-$Na_3Al_2(AsO_4)_3$,[53] which is a member of the above family.

3.6. Electric conductivity measurements. The structural similarity of the $Na_9R(MoO_4)_6$ compounds with the family of arsenates and phosphates indicated in the previous section allows expecting that these molybdates have increased ionic conductivity. This was already confirmed by us in the case of $Na_9Fe(MoO_4)_6$ ($\sigma = 6.8\cdot10^{-2}$ S·cm^{-1} at 800 K).[35]

The temperature dependence of the conductivity is shown in Figure 7 in Arrhenius $\lg(\sigma T)$–$(10^3/T)$ coordinates. Except for the temperature region below 450 K, the conductivity data demonstrate very weak frequency dependence. The reason may be understood from Figure S1 where experimental points on the Z”(Z’) plane lie very tightly along the Z’ axis in the vicinity of the joining of two semi-circulars on the Cole-Cole-type diagrams. It is known[56] that the intersection point of these semi-circulars strictly corresponds to $1/\sigma_{DC}$ – the value of direct-current conductivity of a typical ionic conductor. The measurement of the DC component of the electronic conductivity using the ion blocking method[56] has proved that the electronic contribution (σ_{el}) to the total conductivity in $Na_9Al(MoO_4)_6$ is negligible ($\sigma_{el} << \sigma_{DC}$). Therefore, the electric conductivity in this compound is mainly ionic.

The temperature dependency of the conductivity can be divided into two approximately linear portions with different slopes. The activation energies for these linear portions are ${}^{LT}E_a^{cond}$ ~0.8 eV for the region below 573 K and ${}^{HT}E_a^{cond}$ ~0.6 eV for the high-temperature region. Conductivity values for $Na_9Al(MoO_4)_6$ are as high as $1.52\cdot10^{-3}$ S·cm^{-1} at 573 K and $1.63\cdot10^{-2}$ S·cm^{-1} at 803 K.

The conductivity values for $Na_9Al(MoO_4)_6$ exceed those for II-$Na_{3+x}Fe_2(AsO_4)_3$ ($\sigma = 8\cdot10^{-4}$ S·cm^{-1} at 573 K[51]) but our composition has a larger activation energy of 0.6–0.8 eV against E_a = 0.48 eV.[51] Perhaps, the ionic conductivity characteristics of the obtained compound may be improved by forming solid solutions with isovalent and aliovalent isomorphous substitutions. An interesting variant could be the substitution of MoO_4^{2-} by WO_4^{2-} to form compounds or solid solutions with II-$Na_{3+x}Fe_2(AsO_4)_3$-like structures.

Crystal-chemical analysis shows that the transport of sodium-ions in the structure of $Na_9Fe(MoO_4)_6$ presumably goes through positions Na2 and Na3, involving empty octahedra between RO_6-octahedra, which are translationally identical along the axis *c*.[35] Therefore, Na^+ ion transport in the structure of the studied molybdate probably passes through the Na3, Na4 and Na5 positions related to the Na2 and Na3 positions in $Na_9Fe(MoO_4)_6$. In order to prove this, as well as to determine the causes of the bend at 573 K, the $Na_9Al(MoO_4)_6$ was studied using NMR spectroscopy, the results of which are reported in Sections 3.7 and 3.8. The density functional theory (DFT) calculations required for the NMR data interpretation are presented in the Supplementary Section. As shown in numerous studies (for example, for $NaNbO_3$[57, 58]), *ab initio* methods allow the assignment of NMR lines with a very high accuracy, since the EFG values depend very sensitively on the charge distribution near nuclei.

3.7. NMR: temperature behavior of the ^{23}Na and ^{27}Al spectra. Figure 8*a* shows the temperature behavior of the ^{23}Na NMR spectrum in the $Na_9Al(MoO_4)_6$ oxide over the temperature range 300–750 K. Up to T = 565 K the ^{23}Na NMR spectra consist of two components, each of them is in turn a quadrupole broadened central transition line in the presence of the chemical shift anisotropy. We assign the observed Line-1 (red line in Figure 8*a*) and Line-2 (blue line) to the positions Na1–Na2 and Na3–Na5, respectively. The assignment of the observed lines and the choice of the model for the experimental data approximation are given in more detail in the Supporting information. Figures 9*a–e* represent the temperature dependencies of Line-1 (are shown as filled red circles) and Line-2 (open blue circles) parameters, including data on central line width $\Delta\nu$, quadrupole frequency ν_Q, isotropic shift δ_{iso} and chemical shift anisotropy $\Delta\delta$. Figure 8*b* presents the ^{27}Al NMR spectrum acquired at 750 K. Over the entire temperature range, the NMR signal of ^{27}Al (with spin I = 5/2) consists of five lines: the narrow line corresponding to the central transition, $m_I = -1/2 \leftrightarrow +1/2$, and two pairs of satellite lines corresponding to the transitions $m_I = \pm3/2 \leftrightarrow \pm1/2$ and $\pm5/2 \leftrightarrow \pm3/2$. The ^{27}Al spectra were recorded by the FID method, so their full approximation is difficult (indeed, as seen from Figure 8*b* the satellites appear on the spectrum as some "singularities"), nevertheless the obtained experimental data allow us to estimate with sufficient accuracy the ν_Q and δ_{iso} values.

In the temperature range 300–390 K, a sharp decrease of the central line width is observed for Line-2, $^{(2)}\Delta\nu$ (Figure 9*a*). Such behavior is typical for systems with fast ion diffusion.[59,60] Interestingly, the decrease of $^{(2)}\Delta\nu$ is also accompanied by some decrease of the $\Delta\nu$ value for Line-1, $^{(1)}\Delta\nu$, and $\Delta\nu$ value for ^{27}Al nuclei, nevertheless their changes are not so drastic and some intermediate "plateau" appears in the range 390–490 K. With further temperature increase ($490 < T < 565$ K), both $^{(1)}\Delta\nu$ and $^{(2)}\Delta\nu$ increase. This dependence is reminiscent of the "classical" behavior of the NMR signals at the chemical exchange between two non-equivalent positions: the NMR lines corresponding to different sites broaden at first, and then, with increasing temperature, they are "merged" into one broad line.[59] With further temperature increase, a dynamic narrowing of this "merged" line is expected. The $^{(1)}\Delta\nu$ and $^{(2)}\Delta\nu$ increase is accompanied also by sharp decrease of the $\Delta\nu$ value for ^{27}Al nuclei. These results can be explained by the assumption that for $300 < T < 490$ K the Na^+ ion motion occurs exclusively through the Na3–Na5 positions, while sodium in the Na1 and Na2 sites is "activated" (on the NMR frequency scale) only at $T \geq 490$ K. Indeed, the main factor affecting the $\Delta\nu$ is the dipolar internuclear interaction. For a pair of interacting nuclei, it depends on the distance between the nuclei and the orientation of this pair with respect to the external magnetic field. Atomic jumps lead to changes in both the distance and the orientation. As a result, with increasing temperature and increasing ion jump frequency, the dipolar interaction is averaged and a sharp decrease of the $\Delta\nu$ value is expected.[59,60] In the case of $Na_9Al(MoO_4)_6$, only the ^{23}Na and ^{27}Al can be considered as possible interacting nuclei, while the influence of other NMR isotopes can be neglected due to their low gyromagnetic ratios and natural abundance. The crystal structure of $Na_9Al(MoO_4)_6$ exhibits a different local environment for the ions in the Na1–Na2 and Na3–Na5 positions: the nearest neighbor for Na1–Na2 is Al at a distance $r \sim 3.2$ Å, whereas the nearest sodium ions (in the Na3–Na5 positions) are placed at a distance $r > 3.6$ Å for Na2 and $r > 3.8$ Å for Na1. On the contrary, for the Na3–Na5 sites the nearest neighbors are the ions of the same type (Na3–Na5): one at $r \sim 2.8$–3.1 Å, and 6 at $r \sim 3.6$–4.1 Å. In this case the activation of Na3–Na5 ions at $T \sim 300$ K leads to almost full averaging of the dipolar interaction (which is proportional to r^{-6}) for these ions and to only a partial averaging for Na1–Na2 sites (due to remaining Na–Al interaction). This causes the formation of a plateau on the temperature dependencies of $^{(1)}\Delta\nu$ and $\Delta\nu$ for ^{27}Al nuclei. At the same time, the involvement of Na1–Na2 ions in the fast chemical exchange Na1–Na2 ↔ Na3–Na5 at $T \approx 490$ K leads to a significant decrease of the $\Delta\nu$ value for ^{27}Al.

Nevertheless, unlike the data on $\Delta\nu(T)$, which can easily be described within the framework of the ion diffusion model proposed above, the behavior of other ^{23}Na NMR parameters is hard to explain. . Indeed, at fast ion exchange between two nonequivalent sites, not

only $\Delta\nu$ but also other spectral parameters, such as quadrupole frequency and isotropic shift, must be "merged". The expected values of $\langle\nu_Q\rangle$ and $\langle\delta_{iso}\rangle$ for the merged signal are determined by the probability of finding the ion in a distinct position and the value of the corresponding parameters in the "rigid lattice" (i.e., in the absence of atomic motion). For $\Delta\delta$ the situation is more complicated because this value also depends on the magnetization, which in turn decreases with temperature following the Curie-Weiss law. Thus, for example, the average value of the quadrupole frequency [61,62] after the "merging" of two lines is determined by the relation: $\langle\nu_Q\rangle = [p^{(1)}\nu_{QRL}^{(1)} + p^{(2)}\nu_{QRL}^{(2)}]$. For the ionic jumps with equal probabilities, the $p^{(1)}$ and $p^{(2)}$ values are determined by the filling of the corresponding positions (in our case 0.33 and 0.67 for Na1–Na2 and Na3–Na5 sites, respectively). Taking into account the values of $\nu_{QRL}^{(1)} \approx 1350$ kHz and $\nu_{QRL}^{(2)} \approx 600$ kHz, the expected value $\langle\nu_Q\rangle \approx 850$ kHz. As can be seen from Figure 9*b*, the experimental value $\langle\nu_Q\rangle = 450\pm50$ kHz at $T > 565$ K, is substantially lower than the expected value. Similar effects were also observed for $\langle\delta_{iso}\rangle = -10.4\pm0.3$ ppm at $T > 565$ K, which is again significantly lower than the expected value $\langle\delta_{iso}\rangle \approx -8.4$ ppm (Figure 9*c*).

The deviation of the experimentally observed values for $\langle\nu_Q\rangle$ and $\langle\delta_{iso}\rangle$ from those expected could be explained to some extent by different probabilities of ion jumps between two types of sites.[63,64] Since the $p^{(1)}$ and $p^{(2)}$ values depend on the residence time of the ion in the corresponding positions $\tau_d^{(1)}$ and $\tau_d^{(2)}$, we can assume that $\tau_d^{(2)} > \tau_d^{(1)}$. Thus, leaving the Na1–Na2 site, the Na^+ ion performs a sufficiently large number of jumps within the sublattice of Na3–Na5 positions before it again falls into the vacant Na1–Na2 site. However this way of thinking leads us to a contradictory conclusion that at T > 565 K all Na1–Na2 ions are located in the Na3–Na5 sublattice. Indeed, in our case the values of $\langle\nu_Q\rangle$ and $\langle\delta_{iso}\rangle$ for the merged signal are almost equal to those for Line-2. It means that, $\tau_d^{(2)} >> \tau_d^{(1)}$, and implies that once a Na^+ ion appears in the Na3–Na5 sites sublattice, it will be retained there. It is rather difficult to imagine the physical picture for the implementation of such a scenario, since the already completely filled Na3–Na5 sublattice would have to additionally accommodate ions from Na1–Na2 sites (i.e. another 50% of its initial value). Nevertheless, this paradoxical assumption is supported directly by the temperature dependence of the relative intensity for Line-1 (Figure 9*e*), which decreases at T > 500 K (this line completely disappears at T $\approx$ 565 K).

A possible explanation for the disappearance of Line-1 could be the presence of a phase transition (e.g. of polymorphic type) in the temperature range 500–565 K. As a result, the local surrounding of sodium ions in positions Na1–Na2 becomes similar to that observed for Na3–Na5, and Lines 1 and 2 become indistinguishable. Nevertheless, the distortions of $Na1(Na2)O_6$ octahedra will induce changes in the local coordination of the adjacent Al (see Figure 6*b*). In this case the non-monotonic behavior of $\nu_Q(T)$ and $\delta_{iso}(T)$ for the ^{27}Al nuclei can be expected in this

temperature region. However, with increasing *T*, only a monotonic decrease of ν_Q and an increase in δ_{iso} are observed (see Figure 9*b, c*). Both effects are most likely due to the lattice expansion with temperature. Thus, the ^{27}Al NMR data indicate the absence of any phase transitions in the $Na_9Al(MoO_4)_6$ system over the entire temperature range 300–750 K.

The most probable scenario allowing to describe the disappearance of Line-1 is based on the assumption that the chemical exchange of Na1–Na2 ↔ Na3–Na5 is carried out not directly but through some intermediate position Na^{int}: before the complete jump Na1–Na2 → Na3–Na5, the Na^+ ion performs several local (back and forth) jumps Na1–Na2 ↔ Na^{int}. In this case, the final values of $\langle\nu_Q\rangle$ и $\langle\delta_{iso}\rangle$ can be significantly shifted from the expected ones, since they will depend not on the "rigid lattice" values $\nu_{QRL}^{(1)}$ and $\delta_{isoRL}^{(1)}$, but rather on the values which are already averaged due to Na1–Na2 ↔ Na^{int} jumps. It has to be noted that the jumps within the Na3–Na5 sublattice also most likely occur through some intermediate sites because the $Na3O_6$–$Na5O_6$ octahedra share edges but not faces. However the residence time of ions in these intermediate positions is negligible compared to the time in Na3–Na5 sites, so it does not affect the parameters of the corresponding NMR signal.

Besides clarifying the mechanisms of ion transport, the temperature behavior of the NMR spectra also enables estimating the parameters of ion diffusion, in particular, the characteristic ion jump frequency, τ_d^{-1}, and the activation energy for ion diffusion, E_a. As expected,[59] the dynamic narrowing of the NMR spectrum occurs at a temperature where the ion jump frequency becomes comparable with the "rigid lattice" line width $\tau_d^{-1} \sim 2\pi\Delta\nu_{RL}$. Unfortunately, the investigated temperature range is insufficient to reveal the exact values of $\Delta\nu_{RL}$ (this would need data at T < 300 K). However, this value can be roughly estimated from structural considerations, in particular, form the second moment of the NMR line ($\langle\Delta\omega^2\rangle$) which is known to be determined by Van Vleck's expression.[65] (see Supporting information).We have already considered the features of the nearest environment of Na1–Na2 and Na3–Na5 ions. Summation over the eight nearest neighbors gives, on average, a value of $\langle\Delta\omega^2\rangle \sim 2–3\cdot10^7$ s^{-2}, which in turn yields $\Delta\nu_{RL} \sim 1$ kHz. So, our estimates for $\Delta\nu_{RL}$ coincide in order of magnitude with the measured values of $\Delta\nu \approx 1.5$ kHz at room temperature, which allows us to assume that we are not so far from the "rigid lattice" region. This, in turn, makes it possible to estimate the Na^+ ion jump frequency over the Na3–Na5 positions as $\tau_d^{-1} \sim 10^3–10^4$ s^{-1} already at $T \sim 300$ K. Similarly, taking into account the temperature of the $\Delta\nu$ decrease for ^{27}Al (which corresponds to the activation of Na1–Na2 sites) we can estimate $\tau_d^{-1} \sim 10^3–10^4$ s^{-1} at $T \approx 490$ K for the exchange Na1–Na2 ↔ Na3–Na5.

There are several approaches for the analysis of the $\Delta\nu(T)$ dependence allowing to estimate the E_a value.[59,66–68] The simplest phenomenological approach proposed by Waugh and Fedin[67], suggests that:

$$E_a(\text{meV}) = 1.617 T_0(\text{K}), \quad (1)$$

where T_0 is the temperature of the dynamic narrowing onset. Assuming a value of $T_0 \leq 300$ K, Eq. (1) yields the value $E_a \leq 0.49$ eV for Na^+ jumps within the Na3–Na5 sublattice. For Na1–Na2 ↔ Na3–Na5 jumps we get $E_a \approx 0.8$ eV taking into account the T_0 on the $\Delta\nu(T)$ dependence for ^{27}Al (≈ 490 K).

3.8. NMR: spin-lattice relaxation rate of the ^{23}Na. For the entire studied temperature range 300–750 K, the ^{23}Na spin-lattice relaxation, T_1^{-1}, was characterized by the presence of two components: the slow (T_{1S}^{-1}) and the fast (T_{1F}^{-1}) one. The appearance of two relaxation "branches" is induced most likely by the quadrupole effects in nuclear spin-lattice relaxation. More details of the nuclear magnetization recovery features and estimates of the $T_{1S(F)}^{-1}$ are present in the Supporting information. Figure 10 shows the temperature dependence of $T_{1S(F)}^{-1}$ measured in a magnetic field of 11.7 T.

As can be seen from the presented data, both T_{1F}^{-1} and T_{1S}^{-1} components exhibit a maximum at $T_{max} \approx 585$ K. The appearance of such a maximum on the $T_1^{-1}(T)$ dependence is typical for systems with fast ion diffusion. The simplest model for describing the "dynamic" contribution to T_1^{-1} proposed by Bloembergen, Purcell and Pound (BPP)[69] (see the Supporting information). The results of the fitting of experimental data on T_{1S}^{-1} are shown in Figure 9 as a green dashed line. The fitting parameters are $E_a = 0.47 \pm 0.02$ eV, $\tau_{d0} \approx 1–2 \cdot 10^{13}$ s^{-1}, $\nu_Q \approx 110$ kHz. As can be seen from the presented data, the BPP model does not allow us to describe in full extent the experimental results. The T_1^{-1} temperature dependence is characterized by some asymmetry: the high-temperature slope is deeper than the low-temperature one. Improved models have been developed for the treatment of such asymmetric T_1^{-1} temperature dependences, assuming some distribution of the E_a values (usually in the form of a Gaussian distribution[70–72]), or using spectral density functions of more complex forms (such as Cole-Cole or Cole-Davidson [73,74]). Moreover, our estimates of $E_a \approx 0.47$ eV are significantly lower than the values obtained from the high- and low-temperature "branches" of σT *vs* T^{-1} dependence: $^{HT}E_a^{cond} \sim 0.6$ and $^{LT}E_a^{cond} \sim 0.8$ eV, respectively (Figure 7). The simplest and most suitable model for description of both these effects is the so-called "coupling model" proposed by Ngai (see the Supporting information).[61,75–79] The main idea of this approach is based on the assumption that at low temperatures the motion is slowing down due to the interaction of the diffusing ion with other ions. In this case, E_a^{NMR} is expected to be close to the real value of the energy barrier for the

elementary jump, E_a, whereas E_a^{cond} is overestimated due to the correlation effects in ion motion. The results of fitting the experimental data on T_{1S}^{-1} and T_{1F}^{-1} are shown in Figure 10 as black solid lines. The obtained parameters are E_a^{NMR} = 0.53±0.02 eV, β = 0.64±0.04, $\tau_{d0} \approx 3–4 \cdot 10^{13}$ s^{-1}, $\nu_Q \approx$ 130 and 190 kHz (for T_{1S}^{-1} и T_{1F}^{-1}, respectively). Finally, we tried to approximate the data on T_{1S}^{-1} and T_{1F}^{-1} simultaneously. In general case, the values of T_{1S}^{-1} and T_{1F}^{-1} are determined by more complicated ratios of the probabilities for quantum transitions $\Delta m_I = 1$ and $\Delta m_I = 2$ induced by both quadrupole and dipolar interactions.[80–82] (see the Supporting information). The fit results of the experimental data on T_{1S}^{-1} and T_{1F}^{-1} are shown in Figure 10 as red solid lines. The parameters are close to those obtained previously: E_a^{NMR} = 0.53±0.02 eV, β = 0.64 ±0.04, $\tau_{d0} \approx 3 \cdot 10^{13}$ s^{-1}, $\nu_Q \approx$ 150 kHz. The Inset of Figure 10 shows the estimates of ion jump frequencies, τ_d^{-1}, obtained from these models. It can be seen that our "theoretical" predictions are in good agreement with the "experimental" estimates of $\tau_d^{-1} \sim 10^3–10^4$ s^{-1} at $T \sim$ 300 K and $\tau_d^{-1} \sim 10^9$ s^{-1} at $T \approx$ 585 K, obtained from the analysis of the temperature dependence $^{(1)}\Delta\nu(T)$ and the position of $(T_{1S(F)}^{-1})_{max}$. Therefore, we can ascribe the observed maximum of the spin-lattice relaxation rate to Na^+ ion jumps within the Na3–Na5 positions, which induce the Line-1 narrowing at T = 300 K (see Section 3.7). The maximum of T_1^{-1} corresponding to the Na1–Na2 ↔ Na3–Na5 jumps should be expected at $T \sim$ 1000 K. This can be seen from the Inset of Figure 10 where the blue dashed line represents the predicted values of τ_d^{-1} for the Na1–Na2 ↔ Na3–Na5 exchange obtained from BPP model taking the values of $\tau_{d0} \sim 10^{13}$ s^{-1} and $E_a \approx$ 0.8 eV, which were estimated from an analysis of the data on $\Delta\nu(T)$ for ^{27}Al nuclei (Section 3.7)

In the framework of the coupling model, the expected value for $^{LT}E_a^{cond} \equiv E_a^{NMR}/\beta \approx$ 0.82 eV, that in principle coincides with the result $^{LT}E_a^{cond} \approx$ 0.8 eV obtained from the $\sigma T(1/T)$ dependence at $T <$ 575 K (Figure 7). However some discrepancy exists in the region $T >$ 575 K. On the one hand, in this temperature range the $^{HT}E_a^{cond}$ ~0.6 eV should be equal to E_a^{NMR} =0.53 eV [63]. On the other hand, our E_a^{NMR} estimates obtained from T_1^{-1} analysis are slightly higher than those obtained from the $\Delta\nu(T)$ analysis: $E_a \leq$ 0.49 eV according to Eq. (1) (Section 3.7). This discrepancy can be explained in two different ways. On the one hand, a lower E_a^{NMR} compared with $^{HT}E_a^{cond}$ may indicate that the correlation effects in the Na motion in $Na_9Al(MoO_4)_6$ do not disappear even at the highest temperatures. On the other hand, the obtained E_a^{NMR} estimates can be somewhat underestimated. Indeed, Eq. (1) can in principle give a substantial error (especially if we take into account the presence of any correlation effects in the sodium motion), so that the real value of E_a can be significantly higher. Moreover, the E_a^{NMR} estimated from the $T_{1S(F)}^{-1}(T)$ analysis can also be somewhat underestimated due to the influence of the second maximum $T_{1S(F)}^{-1}$ associated with the Na1–Na2 ↔ Na3–Na5 jumps. As it is already noted, the corresponding maximum should be observed at $T \sim$ 1000 K, so the data on the high-temperature

slope of the revealed relaxation rate peak (at $T > 600$ K) can be distorted by the influence of the low-temperature slope of this second $T_{1S(F)}^{-1}$ maximum**.** In this situation, we can estimate the values of the activation energy as $E_a = 0.55 \pm 0.05$ eV and ≈ 0.8 eV for Na^+ ions jumps within the sublattices of the positions Na3–Na5 and for jumps Na1–Na2 ↔ Na3–Na5, respectively.

Thus, on the basis of the structure, NMR and conductivity data, some general remarks about the microscopic model for the Na^+ motion in $Na_9Al(MoO_4)_6$ can be made. In particular, the activation of the Na3–Na5 positions at lower temperatures is most likely due to substantially shorter jump lengths: the distance to the nearest sites is $r \sim 2.8$–3.1 Å for Na3–Na5, and exceeds 3.6–3.8 Å for Na(1–2)–Na(3–5). The same reason governs most likely the absence of direct jumps within the Na1–Na2 sublattice, here the distances are even longer (≥ 5 Å). Moreover, for such jumps, the Coulomb repulsion of two adjacent highly charged Mo^{6+} ions has to be overcome (Figures 6*b* and 11). So, the only possible way for these ions to be involved in diffusion processes is the chemical exchange with the subsystem of Na3–Na5 sites (Figure 12). The correlation effects slowing down the Na diffusion in the Na3–Na5 sites sublattice at $T < 575$ K are induced most likely by the "static" (on the NMR frequency scale) Na1–Na2 ions. Indeed, the bend point on $\sigma T(T^{-1}) \approx 575$ K is close to the temperature of the Line-1 disappearance (≈ 565 K). Moreover, the ${}^{LT}E_a^{cond}$ value is close to the activation energy of the Na1–Na2 ions. Thus, it can be assumed that the correlation effects in the motion along the Na3–Na5 sites disappear when the Na1–Na2 ions become highly involved in the diffusion. The release of Na1–Na2 sites causes not only the appearance of vacant places available for jumping Na3–Na5 ions but induces most likely the small displacements of the adjacent Mo^{6+} ions from their equilibrium positions. The combination of both these effects leads to a decrease of Coulomb repulsion and as a result to reduction of the effective E_a. The disappearance of correlation effects in ionic motion due to the change of site occupancy were observed before, in particular for the compound $Li_{1.2}Ti_{1.8}Al_{0.2}(PO_4)_3$.[61]

Summarizing the NMR results, the temperature behavior of the ^{23}Na and ^{27}Al NMR spectra and the spin-lattice relaxation rates of ^{23}Na nuclei indicate the presence of rather fast Na^+ ion diffusion in the studied compound. At temperatures below 490 K, diffusion occurs by means of ion jumps exclusively through the sublattice of Na3–Na5 positions (Figure 12*a*). Estimates of the of atomic jump frequencies yield a value of $\tau_d^{-1} \sim 10^3$–10^4 s^{-1} at $T \sim 300$ K and $\sim 10^9$ s^{-1} at $T \sim$ 600 K. Estimates of the activation energy for ion diffusion give the value of $E_a \approx 0.55$ eV. Up to $T \sim 570$ K, the Na3–Na5 jumps are characterized by the presence of strong correlation effects, which are most likely due to the presence of static (on the NMR frequency scale) ions in the Na1–Na2 sites. The Na1–Na2 become involved in the diffusion processes (through the chemical

exchange with the Na3–Na5 sublattice) only at $T > 490$ K (Figure 12*b*). The parameters for Na1–Na2 ↔ Na3–Na5 jumps are $\tau_d^{-1} \sim 10^3$–10^4 s^{-1} at $T \sim 500$ K, $E_a \approx 0.8$ eV.

4. CONCLUSION

A novel double molybdate $Na_9Al(MoO_4)_6$ was synthesized by a solid state reaction and studied by PXRD and TEM. The sample crystallized in monoclinic symmetry with *C*2/*c* space group and the unit cell parameters are $a = 15.4067(3)$, $b = 14.6428(3)$, $c = 10.6250(2)$ Å, $\beta = 93.991(2)°$. The structure has an open framework where the Na^+ ions are located. Impedance spectroscopy measurements show that $Na_9Al(MoO_4)_6$ is an ionic conductor with a conductivity $1.63 \cdot 10^{-2}$ $S \cdot cm^{-1}$ at 803 K. NMR experiments indicate the presence of fast Na^+ ion diffusion in the obtained compound. At low temperatures, diffusion occurs by means of ion jumps through the sublattice of Na3–Na5 positions, the Na1–Na2 become involved in the diffusion processes only at high temperatures.

Supporting Information

The Supporting Information is available free of charge on the ACS Publications website. Table S1–S3, Figure S1–S3; Sections: ^{23}Na NMR at room temperature: assignment of different spectral components to the distinct positions of Na^+ ions in the $Na_9Al(MoO_4)_6$; Second moment of the NMR line; Spin-lattice relaxation rate of the ^{23}Na; The BPP model for describing the "dynamic" contribution to T_1^{-1}; The "coupling model".

Acknowledgments

The research was carried out within the state assignment of FASO of Russia (Themes No 01201463330, No A16-116122810214-9 and No 0339-2016-0007), supported in part by the Russian Foundation for Basic Research (Projects No. 16-03-00510, 16-03-00164, 17-03-00333)

References

(1) Minami, T.; Imazawa, K.; Tanaka, M. Formation region and characterization of superionic conducting glasses in the systems AgI–Ag_2O–M_xO_y. *J. Non-Cryst. Solids* **1980**, 42, 469–476.

(2) Maruyama, T.; Sasaki, S.; Saito, Y. Potentiometric gas sensor for carbon dioxide using solid electrolytes. *Solid State Ion.* **1987**, 23, 107–112.

(3) Laskar, A. L.; Chandra S. (Eds.), Superionic Solids and Solid Electrolytes - Recent Trends, Academic Press, San Diego, **1989**.

(4) Chowdari, V. R.; Radhakrishna S. (Eds.), Materials for Solid State Batteries, World Scientific, Singapore, **1986**.

(5) Steele, B.C.H.; Heinzel, A. Materials for fuel-cell technologies, *Nature*. **2001,** 414, P. 345–352.

(6) Linford, R.; Schlindwein, W. Medical applications of solid state ionics. *Solid State Ionics*, **2006,** 177, 1559–1565.

(7) Moore, P. B. Crystal chemistry of the alluaudite structure type: contribution to the paragenesis of pegmatite phosphate giant crystals. *Am. Mineral.* **1971**, 56, 1955–1975.

(8) Gao J., Pan Zhao P.; Feng K. $Na_{2.67}Mn_{1.67}(MoO_4)_3$: A 3.45 V Alluaudite-Type Cathode Candidate for Sodium-Ion Batteries, *Chem. Mater*., **2017**, 29, 940–944

(9) Evdokimov, A. A.; Efremov, V. A.; Trunov, V. K.; Kleiman, I. A.; Djurinsky, B. F. Soedineniya Redkozemel- nykh Elementov. Molibdaty. Volframaty [Rare-earth Compounds. Molyb dates, Tungstates], Nauka, Moscow, **1991,** 267 pp. (in Russian).

(10) Trunov, V. K.; Efremov, V. A.; Velikodny, Yu. A. I. Kristallokhimiya, Svoistva Dvoinykh Molibdatov i Volframatov [Crystal Chemistry and Properties of Double Molybdates and Tungstates], Nauka, Leningrad, **1986**, 173 pp. (in Russian).

(11) Isupov, V. A. Binary Molybdates and Tungstates of Mono and Trivalent Elements as Possible Ferroelastics and Ferroelectrics. *Ferroelectrics* 2005, 321, 63–90.

(12) Tkáč, V.; Orendáčová, A.; Čižmár, E.; Orendáč, M.; Zvyagin, S.; Anders, A. G.; Pavlík, V.; Feher, A. Experimental study of magnetic anisotropy in a layered $CsNd(MoO_4)_2$. *J. Alloy. Comp.* **2014**, 591, 100–104.

(13) Mączka, M.; Ptak, M.; Luz-Lima, C.; Freire, P. T. C.; Paraguassu, W.; Guerini, S.; Hanuza, J. Pressure-induced phase transitions in multiferroic $RbFe(MoO_4)_2$ – Raman scattering study. *J. Solid State Chem.* **2011**, 184, 2812–2817.

(14) Sarapulova, A.; Mikhailova, D.; Senyshyn, A.; Ehrenberg, H. Crystal structure and magnetic properties of Li,Cr-containing molybdates $Li_3Cr(MoO_4)_3$, $LiCr(MoO_4)_2$ and $Li_{1.8}Cr_{1.2}(MoO_4)_3$. *J. Solid State Chem*. **2009**, 182, 3262–3268.

(15) Guo, F.; Ru, J.; Li, H.; Zhuang, N.; Zhao, B.; Chen, J. Growth and magneto-optical properties of $NaTb(MoO_4)_2$ crystals. *J. Cryst. Growth* **2008**, 310, 4390–4393.

(16) Lin, Z.; Xu, M.; Hong, Y.; Wang, X.; Fu, P. Surfactant-free hydrothermal synthesis and gas-sensing properties of $NaBi(MoO_4)_2$ nanocrystals. *Mater. Lett.* **2016**, 168, 72–75.

(17) Yan, X.; Wang, X.; Gu, W.; Wu, M.; Yan, Y.; Hu, B.; Che, G.; Han, D.; Yang, J.; Fan, W., Shi, W. Single-crystalline $AgIn(MoO_4)_2$ nanosheets grafted Ag/AgBr composites with enhanced plasmonic photocatalytic activity for degradation of tetracycline under visible light. *Appl. Catal. B Environ*. **2015**, 164, 297–304.

(18) Arakcheeva, A. V.; Logvinovich, D.; Chapuis, G.; Morozov, V. A.; Eliseeva, S. V.; G.Bünzli, J.-C.; Pattison, P. Pattison The luminescence of $Na_xEu^{3+}_{(2-x)/3}MoO_4$ scheelites depends on the number of Eu-clusters occurring in their incommensurately modulated structure. *Chem. Sci*. **2012**, 3, 384–390.

(19) Morozov, V. A.; Lazoryak, B. I.; Shmurak, S. Z.; Kiselev, A. P.; Lebedev, O. I.; Gauquelin, N.; Verbeeck, J.; Hadermann, J.; Van Tendeloo, G. Influence of the Structure on the Properties of $Na_xEu_y(MoO_4)_z$ Red Phosphors. *Chem. Mater.* **2014**, 26, 3238–3248.

(20) Loiko, P. A.; Han, X.; Yumashev, K. V.; Kuleshov, N. V.; Serrano, M. D.; Cascales, C.; Zaldo, C. Thermo-optical properties of uniaxial $NaT(XO_4)_2$ laser host crystals (where T = Y, La, Gd or Bi, and X = W or Mo). *Appl. Phys. B Lasers Opt.* **2013**, 111, 279–287.

(21) Hwang, K.-S.; Kang, B.-A.; Hwangbo, S.; Kim, Y.-S.; Kim, J.-T. Low-temperature synthesis of $LiEuMo_2O_8$ red phosphor for a white-light-emitting diode. *Electron. Mater. Lett.* **2010**, 6, 27–30.

(22) Benoît, G.; Véronique, J.; Arnaud, A.; Alain, G. Luminescence properties of tungstates and molybdates phosphors: Illustration on $ALn(MO_4)_2$ compounds (A = alikaline cation, Ln = lanthanides, M = W, Mo). *Solid State Sci.* **2011**, 13, 460–467.

(23) Liu, Y.; Zuo, H.; Li, J.; Shi, X.; Ma, S.; Zhao, M.; Zhang, K.; Wang, C. Hydrothermal synthesis and multicolor luminescence properties of Dy^{3+}/Eu^{3+} co-doped $KLa(MoO_4)_2$ phosphors. *Ceram. Int.* **2016**, 42, 7781–7786.

(24) Zuo, H.; Liu, Y.; Li, J.; Shi, X.; Ma, S.; Zhao, M. Enhancement of red emission in $KLa(MoO_4)_2$:Eu^{3+}, Bi^{3+} phosphor for WLEDs. *Ceram. Int.* **2015**, 41, 14834–14838.

(25) Wang, Q.-F.; Liu, Y.; Wang, Y.; Wang, W.; Wan, Y.; Wang, G.-G.; Lu, Z.-G. Considerable photoluminescence enhancement of $LiEu(MoO_4)_2$ red phosphors via Bi and/or Si doping for white LEDs. *J. Alloy. Comp.* **2015**, 625, 355–361.

(26) Yan, J.; Xiao, X.; Yu, J.; Mao, D.; Lu, G. White light emission materials of self-assembled rare earth molybdates $NaRE(MoO_4)_2$ micro-particles: the controllable synthesis, growth mechanism and luminescent properties. *Cryst. Res. Technol.* **2015**, 50, 580–593.

(27) Li, L.; Zhang, J.; Zi, W.; Gan, S.; Ji, G.; Zou, H.; Xu, X. Synthesis and luminescent properties of high brightness $MRE(MoO_4)_2:Eu^{3+}$ (M = Li, Na, K; RE = Gd, Y, Lu) red phosphors for white LEDs. *Solid State Sci.* **2014**, 29, 58–65.

(28) Park, S. W.; Noh, H. M.; Moon, B. K.; Choi, B. C.; Jeong, J. H.; Yang, H. K. Hydrothermal synthesis and photoluminescence investigation of $NaY(MoO_4)_2:Eu^{3+}$ nanophosphor. *J. Nanosci. Nanotechnol.* **2014**, 14, 8724–8728.

(29) Wang, Y.; Lin, C.; Zheng, H.; Sun, D.; Li, L.; Chen, B. Fluorescent and chromatic properties of visible-emitting phosphor $KLa(MoO_4)_2:Sm^{3+}$. *J. Alloy. Comp.* **2013**, 559, 123–128.

(30) Wang, Z.; Liang, H.; Wang, Q.; Luo, L.; Gong, M. Luminescent properties of Tb3+ activated double molybdates and tungstates. *Mater. Sci. Eng. B* **2009**, 164, 120–123.

(31) Maczka, M.; Hermanowicz, K.; Tomaszewski, P. E.; Zawadzki, M.; Hanuza, J. Vibrational and luminescence studies of $MIIn(MoO_4)_2$ (MI = K, Rb) and $MIAl(MoO_4)_2$ (MI = K, Na) molybdates doped with chromium(III) prepared via the Pechini method. *Opt. Mater.* **2008**, 31, 167–175.

(32) Wang, Z.; Liang, H.; Gong, M.; Su, Q. Luminescence investigation of Eu^{3+} activated double molybdates red phosphors with scheelite structure. *J. Alloy. Comp.* **2007**, 432, 308–312.

(33) Balda, R.; Fernández, J.; Iparraguirre, I.; Al-Saleh, M. Spectroscopic study of Nd^{3+}/Yb^{3+} in disordered potassium bismuth molybdate laser crystals. *Opt. Mater.* **2006**, 28, 1247–1252.

(34) Voron'ko, Yu. K.; Subbotin, K. A.; Shukshin, V. E.; Lis, D. A.; Ushakov, S. N.; Popov, A. V.; Zharikov, E. V. Growth and spectroscopic investigations of Yb^{3+}-doped $NaGd(MoO_4)_2$ and $NaLa(MoO_4)_2$ – new promising laser crystals. *Opt. Mater.* **2006**, 29, 246–252.

(35) Savina, A. A.; Solodovnikov, S. F.; Basovich, O. M.; Solodovnikova, Z. A.; Belov, D. A.; Pokholok, K. V.; Gudkova, I. A.; Stefanovich, S. Yu.; Lazoryak, B. I.; Khaikina, E. G. New double molybdate $Na_9Fe(MoO_4)_6$: synthesis, structure, properties. *J. Solid State Chem*. **2013**, 205, 149–153.

(36) Velikodny, Yu. A. PhD Thesis (Chemistry) **1975**, 121.

(37) Savina, A. A.; Morozov, V. A.; Basovich, O. M.; Khaikina, E. G.; Lazoryak, B.I. Double molybdate $Na_9Sc(MoO_4)_6$. *Acta Cryst.* **2013**, C69, 1301–1303.

(38) Dridi, W.; Ennajeh, I.; Zid, M. F. Synthése et étude structurale de $Na_9Cr(MoO_4)_6$. *Acta Cryst.* **2015**, E71, 435–439.

(39) Sonni, M.; Marzouki, R.; Zid, M. F.; Souilem, A. Elaboration, étude structurale et analyse CHARDI et BVS d`une nouvelle variété β-$Na_9Cr(MoO_4)_6$ de type alluaudite. *Acta Cryst.* **2016**, E72, 833–837.

(40) Le Bail, A.; Duroy, H.; Fourquet, J. L. Ab-initio structure determination of $LiSbWO_6$ by X-ray powder diffraction. *Mater. Res. Bull.* **1988**, 23, 447–452.

(41) Petricek, V.; Dusek, M.; Palatinus, L. Crystallographic Computing System JANA2006: General features. *Z. Kristallogr.* **2014**, 229(5), 345–352.

(42) Momma, K.; Izumi, F. VESTA 3 for three-dimensional visualization of crystal, volumetric and morphology data. *J. Appl. Crystallogr.* **2011**, 44, 1272–1276.

(43) Belik, A. A.; Izumi, F.; Ikeda, T.; Morozov, V. A.; Dilanian, R. A.; Torii, S.; Kopnin, E. M.; Lebedev, O. I.; Van Tendeloo, G.; Lazoryak, B. I. Positional and Orientational Disorder in a Solid Solution of $Sr_{9+x}Ni_{1.5-x}(PO_4)_7$ (x = 0.3) *Chem. Mater.* **2002**, 14, 4464–4472.

(44) Kurtz, S. K.; Perry, T. T. A Powder Technique for the Evaluation of Nonlinear Optical Materials. *J. Appl. Phys.* **1968**, 39, 3798–3812.

(45) Massiot, D.; Fayon, F.; Capron, M.; King, I.; Le Calve, S.; Alonso, B.; Durand, J.-O.; Bujoli, B.; Gan, Zh.; Hoatson, G. Modelling one- and two-dimensional solid-state NMR spectra. *Magn. Reson. Chem.* 2002, 40, 70–76.

(46) Kresse, G.; Joubert, D. From ultrasoft pseudopotentials to the projector augmented-wave method *Phys. Rev. B* 1999, 59, 1758–1775. Kresse, G.; Furthmüller, J. *Phys. Rev. B* **1996**, 54, 11169.

(47) Kresse, G.; Hafner, J. *Ab initio* molecular dynamics for liquid metals. *Phys. Rev. B* 1993, 47, 558–561.

(48) Perdew, J. P.; Burke, K.; Ernzerhof, M. Generalized gradient approximation made simple. *Phys. Rev. Lett.* 1996, 77, 3865–3868.

(49) Monkhorst, H. J.; Pack, J. D. Special points for Brillouin-zone integrations. *Phys. Rev. B* **1976**, 13, 5188–5192.

(50) Rietveld, H. M. A profile refinement method for nuclear and magnetic structures. *J. Appl. Cryst.* **1969**, 2, 65–71.

(51) D'Yvoire, F.; Bretey, E.; Collin, G. Crystal structure, non-stoichiometry and conductivity of II-$Na_3M_2(AsO_4)_3$ (M = Al, Ga, Cr, Fe). *Solid State Ion.* **1988**, 28–30, 1259–1264.

(52) d'Yvoire, F.; Pintard-Screpel, M.; Bretey, E. Polymorphism and cation transport properties in arsenates $Na_3M_2(AsO_4)_3$ (M = Al, Cr, Fe, Ga)**.** *Solid State Ion.* **1986**, 18/19, 502–506.

(53) Masquelier, C.; d'Yvoire, F.; Collin, G. Crystal structure of $Na_7Fe_4(AsO_4)_6$ and α-$Na_3Al_2(AsO_4)_3$, two sodium ion conductors structurally related to II-$Na_3M_2(AsO_4)_3$. *Solid State Chem.* **1995**, 118, 33–42.

(54) Belokoneva, E.L.; Ruchkina, E.A.; Dimitrova, O.V.; Stefanovich, S. Yu. New trigonal $Na_3Fe_2(PO_4)_3$ phase: Synthesis and crystal structure. *Rus. J. Inorg. Chem.* **2002**, 47, 1297–1300.

(55) Lii, K.-H. $Na_7Fe_4(PO_4)_6$: a mixed-valence iron phosphate containing a tetramer of edge-sharing FeO_6 octahedra. *J. Chem. Soc. Dalton Trans.* **1996**, 6, 819–822.

(56) Barsoukov, E.; Macdonald, J. R. Impedance Spectroscopy: Theory, Experiment, and Applications. John Wiley & Sons; Inc. Hoboken (USA), **2005**, 608 pp.

(57) Johnston, K. E.; Tang, C. C.; Parker, J. E.; Knight, K. S.; Lightfoot, P.; Ashbrook, S. E. The Polar Phase of $NaNbO_3$: A Combined Study by Powder Diffraction, Solid-State NMR, and First-Principles Calculations. *J. Am. Chem. Soc.* 2010, **132**, 8732–8746.

(58) Gonçalves J. N.; Stroppa A.; Correia J. G.; Butz T.; Picozzi S.; Fenta A. S.; Amaral V. S. *Ab initio* study of the relation between electric polarization and electric field gradients in ferroelectrics. *Phys. Rev. B* **2012**, 86, 035145.

(59) Abragam, A. The Principles of Nuclear Magnetism. Clarendon Press: Oxford, UK, **1961**, 599 p.

(60) Slichter, C. P. Principles of Magnetic Resonance. Springer-Verlag: Berlin, **1980**, 397 pp.

(61) Arbi, K.; Tabellout, M.; Lazarraga, M. G.; Rojo, J. M.; Sanz, J. Non-Arrhenius conductivity in the fast lithium conductor $Li_{1.2}Ti_{1.8}Al_{0.2}(PO_4)_3$: A ^{7}Li NMR and electric impedance study. *Phys. Rev. B* **2005**, 72, 094302.

(62) Bader, B.; Heitjans, P.; Stockman, H.-J.; Ackerman, H.; Buttlert, W.; Freilander, P.; Kiese, G.; van der Marel, C.; Schirmer, A. Li^+ diffusion in the fast ionic conductor Li_3N investigated by β-radiation detected NMR. *J. Phys: Candens. Matter* **1992**, 4, 4779–4800.

(63) Baklanova, Ya. V.; Denisova, T. A.; Arapova, I. Yu.; Buzlukov, A. L.; Gerashenko, A. P.; Verkhovskii, S. V.; Mikhalev, K. N.; Shein, I. R.; Maksimova, L. G. Localization of vacancies and mobility of lithium ions in Li_2ZrO_3 as obtained by ^{6,7}Li NMR. *J. Solid State Chem.* **2013**, 208**,** 43–49.

(64) Buzlukov, A. L.; Arapova, I. Yu.; Baklanova, Y. V.; Medvedeva, N. I.; Denisova, T. A.; Verkhovskii, S. V. Coexistence of Two Types of Lithium Motion in Monoclinic Li_2HfO_3: ^{6,7}Li NMR and Ab Initio Calculation Results. *J. Phys. Chem. C* **2016**, 120, 23911–23921.

(65) Van Vleck, J. H. The Dipolar Broadening of Magnetic Resonance Lines in Crystals. *Phys. Rev.* **1948**, 74, 1168–1183.

(66) Hendrickson, J. R.; Bray, P. J. A Phenomenological Equation for NMR Motional Narrowing in Solids. *J. Magn. Resonance* **1973**, 9, 341–357.

(67) Waugh, J. S.; Fedin, E. I. On the Determination of Hindered Rotation Barriers in Solids. *Sov. Phys. Solid State* **1963**, 4, 1633–1636.

(68) Wilkening, M.; Bork, D.; Indris, S.; Heitjans, P. Diffusion in amorphous $LiNbO_3$ studied by ^{7}Li NMR – comparison with the nano- and microcrystalline material. *Phys. Chem. Chem. Phys.* **2002**, 4, 3246–3251.

(69) Bloembergen, N.; Purcell, E.M.; Pound, R.V. Relaxation Effects in Nuclear Magnetic Resonance Absorption. *Phys. Rev.* **1948**, 73, 679–715.

(70) Shinar, J.; Davidov, D.; Shaltiel, D. Proton NMR Study of Diffusion in Continuous, non Stoichiometrc Metal Hydrogen Systems HfV_2H_x and ZrV_2H_x. *Phys. Rev. B: Condens. Matter Mater. Phys.* **1984**, 30, 6331–6341.

(71) Sen, S.; Stebbins, J. F. Na-ion transport in borate and germanate glasses and liquids: A ^{23}Na and ^{11}B NMR spin-lattice-relaxation study. *Phys. Rev.* **1997**, 55, 3512–3519.

(72) Svare, I.; Borsa, F.; Torgeson, D. R.; Martin S. W. Correlation functions for ionic motion from NMR relaxation and electrical conductivity in the glassy fast-ion conductor $(Li_2S)_{0.56}(SiS_2)_{0.44}$. *Phys. Rev. B* **1993**, 48, 9336–9344.

(73) Beckmann, P.A. Spectral Densities and Nuclear Spin Relaxation in Solids. *Phys. Reports (Rev. S. Phys. Lett.)* **1988**, 171, 85–128.

(74) Grüne, M.; Müller-Warmuth, W. Considerations and Examples for a Uniform Behaviour of Spin-Lattice Relaxation in Glasses. *Ber. Bunsenges. Phys. Chem.* 1991, 95, 1068–1071.

(75) Kanert, O.; Steinert, J.; Jain, H.; Ngai, K. L. Nuclear spin relaxation and atomic motion in inorganic glasses. *J. Non-Crystalline Solids* **1991**, 131–133, 1001–1010.

(76) Ngai, K. L.; Kanert, O. Comparison between the coupling model predictions, Monte Carlo simulations and some recent experimental data of conductivity relaxation in glassy ionics. *Solid State Ion.* **1992**, 53–56, 936–946.

(77) Ngai, K. L. Analysis of NMR and conductivity-relaxation measurements in glassy Li_2S-SiS_2 fast-ion conductors. *Phys. Rev. B* **1993**, 48, 13481–13485.

(78) Ngai, K. L.; Rizo, A. K. Parameterless Explanation of the Non-Arrhenius Conductivity in Glassy Fast Ionic Conductors. *Phys. Rev. Lett.* **1996**, 76, 1296–1299.

(79) Funke, K. Jump relaxation in solid electrolytes. *Prog. Solid St. Chem.* **1993**, 22, 111–195.

(80) Brinkmann, D.; Mali, M.; Roos, J.; Messer, R.; Birli, H. Diffusion processes in the superionic conductor Li_3N: An NMR study. *Phys. Rev. B* **1982**, 26, 4810–4825.

(81) Hughes, D. G. Non-exponential magnetic relaxation of $I = 3/2$ nuclear spins in solids. *J. Phys.: Condens. Matter*. **1993**, 5, 2025–2032.

(82) Yesinowski, J. P. Finding the true spin–lattice relaxation time for half-integral nuclei with non-zero quadrupole couplings. *J. Magn. Resonance* **2015**, 252, 135–144.

Table 1. Details of the $Na_9Al(MoO_4)_6$ structure refinement

Sample composition		$Na_9Al(MoO_4)_6$	
Formula weight		1193.5	
Cell setting	Trigonal	Trigonal	Monoclinic
Space group	$R\bar{3}c$	$R\bar{3}$	$C2/c$
Lattice parameters:			
a, Å	14.64277(6)	14.64379(6)	15.4067(3)
b, Å			14.6428(3)
c, Å	19.31283(13)	19.31417(13)	10.6250(2)
β, °			93.991(2)
V, Å^3	3586.11(2)	3586.85(3)	2391.16(9)
Density,	3.31591(2)	3.31522(2)	3.31533(7)
Formula units, Z	6	6	4
Color		white	
Data collection			
Diffractometer		Bruker D8 ADVANCE	
Temperature,		293	
Radiation/ Wavelength (λ, Å)		Cu*K*α radiation / λ = 1.5418 Å	
Data collection mode		Reflection	
Scan method		Step	
2θ range (°)		7–100	
Step scan (2θ)		0.02076	
I_{max}		81200	
Number of points		4479	
Refinement			
Refinement		Rietveld	
Background function		Legendre polynomials, 18 terms	
No. of reflections (All/observed)	413/412	820/815	1227/1221
No. of refined parameters/refined atomic parameters	55/28	72/45	92/63
R and R_w (%) for Bragg reflections (R_{all}/R_{obs})	4.12/4.12; 4.92/4.92	3.79/3.75; 4.61/4.60	3.49/3.48; 4.21/4.20
R_P and R_{wP}; R_{exp}	4.72, 6.41, 2.08	4.49, 6.14, 2.07	4.29, 5.94, 2.07
Goodness of fit (ChiQ)	3.09	2.96	2.87
Max./min. residual density	1.36/ -1.20	1.20/ -1.03	1.16/ -0.92

Figure Captions

Figure 1. Part of the PXRD patterns of the $Na_9Al(MoO_4)_6$ in 2θ ranges of 10−18° (*a*) and 47.7−43.4° (*b*). Tick marks denote the peak positions and the indexation of possible Bragg reflections.

Figure 2. ED patterns along the main zone axes for $Na_9Al(MoO_4)_6$: *a*) indexing in the *Cc* or *C2/c* space group (left column); *b*) indexed in the $R\bar{3}c$ space group (right column).

Figure 3. (*Color online*). Transformation of lattice parameters from $R\bar{3}c$ subcell (marked as a_R, b_R, c_R) to monoclinic *C*2/*c* cell (marked as a_m, c_m).

Figure 4. Portions of observed, calculated and difference PXRD patterns for $Na_9Al(MoO_4)_6$. Tick marks denote the peak positions of possible Bragg reflections.

Figure 5. (*Color online*). Projection of the $Na_9Al(MoO_4)_6$ structure (*a*) and a view of the $Na_9Fe(MoO_4)_6$ structure showing only the $[Fe(MoO_4)_6]^{9-}$ clusters (*b*). The large blue spheres and small red spheres indicate Na and oxygen atoms, respectively.

Figure 6. (*Color online*). $[Al(MoO_4)_6]^{9-}$ cluster (*a*) and fragment from $[Al(MoO_4)_6]^{9-}$ cluster and three NaO_6-octahedra in $Na_9Al(MoO_4)_6$ structure (*b*).

Figure 7. (*Color online*). Temperature dependence of the conductivity of $Na_9Al(MoO_4)_6$.

Figure 8. (*Color online*) (*a*) The temperature evolution of the ^{23}Na NMR spectrum in $Na_9Al(MoO_4)_6$ over the temperature range 300–750 K in a magnetic field 11.7 T. Experimental data are shown as black lines, the fitting results by green lines. (*b*) NMR spectrum of ^{27}Al nuclei measured at 750 K in the field 11.7 T.

Figure 9. (*Color online*). Temperature behavior of the ^{23}Na and ^{27}Al NMR signal parameters (11.7 T): (*a*) central line width, $\Delta\nu$, (*b*) quadrupole frequency ν_Q, (*c*) isotropic shift δ_{iso}, *(d)* chemical shift anisotropy $\Delta\delta$, and *(e)* the relative intensities of lines 1 and 2. Filled red and open blue circles correspond to ^{23}Na Line-1 and Line-2, respectively. The black squares correspond to NMR parameters of the signal after the "merging" of lines 1 and 2. Black crosses are the corresponding NMR parameters for ^{27}Al nuclei.

Figure 10. (*Color online*). Arrhenius plot of the ^{23}Na spin-lattice relaxation rate measured in a magnetic field 11.7 T over the temperature range 300–750 K. The filled and empty circles correspond to the slow (T_{1S}^{-1}) and fast (T_{1F}^{-1}) relaxation components. The green dashed line corresponds to the fit of experimental data on T_{1S}^{-1} by the BPP model. Black and red solid lines are the approximations of the data on T_{1S}^{-1} and T_{1F}^{-1} by the coupling model and generalized coupling model, respectively. The inset shows the estimates of τ_d^{-1} for Na^+ jumps in the Na(3–5) sites sublattice, the lines correspond to the fit results by BPP model, coupling model and generalized coupling model. The dots – are the estimates of τ_d^{-1} obtained from the experimental

data on $\Delta\nu(T)$ (○) and $(T_1^{-1})_{max}$ (□). The (●) and dotted line are the estimates of τ_d^{-1} for Na(1–2) ↔ Na(3–5) jumps, obtained from the analysis of the data on $\Delta\nu(T)$ for ^{27}Al and BPP model, respectively.

Figure 11. (*Color online*). Fragment of $[Al(MoO_4)_6]^{9-}$ cluster with NaO_6 octahedra (pale red) and octahedral interstitials (grey) between MoO_4 tetrahedra (pale yellow) representing the blocking jumps within the Na1–Na2 sublattice.

Figure 12. (*Color online*). The scheme of Na^+ transport: *a* – at temperatures below 490 K exclusively by positions Na3–Na5; *b* – above 490 K with the involvement of positions Na1–Na2 through the chemical exchange with Na3–Na5 sublattice.

Table of Contents

Aleksandra A. Savina, Vladimir A. Morozov, Anton L. Buzlukov, Irina Yu. Arapova, Sergey Yu. Stefanovich, Yana V. Baklanova, Tatiana A. Denisova, Nadezhda I. Medvedeva, Michel Bardet, Joke Hadermann, Bogdan I. Lazoryak, Elena G. Khaikina

Chem. Mater.

New Solid Electrolyte $Na_9Al(MoO_4)_6$: Structure and Na^+ Ion Conductivity

This work reports the crystal structure and electrical properties of a new solid electrolyte $Na_9Al(MoO_4)_6$. The structure is related to that of sodium ion conductor II-$Na_3Fe_2(AsO_4)_3$. The conductivity of $Na_9Al(MoO_4)_6$ at T = 803 K equals $\sigma = 1.63 \cdot 10^{-2}$ S·cm^{-1}. The temperature behavior of the ^{23}Na and ^{27}Al NMR spectra and the spin-lattice relaxation rates of the ^{23}Na nuclei indicate the presence of fast Na^+ ion diffusion. At T < 490 K, diffusion occurs by means of ion jumps exclusively through the sublattice of Na3–Na5 positions while the Na1–Na2 only become involved in the diffusion processes at higher temperatures.

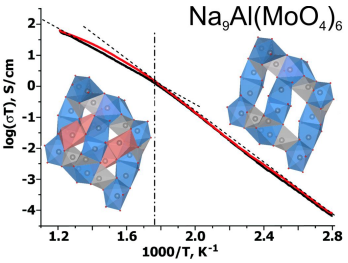

TOC figure.

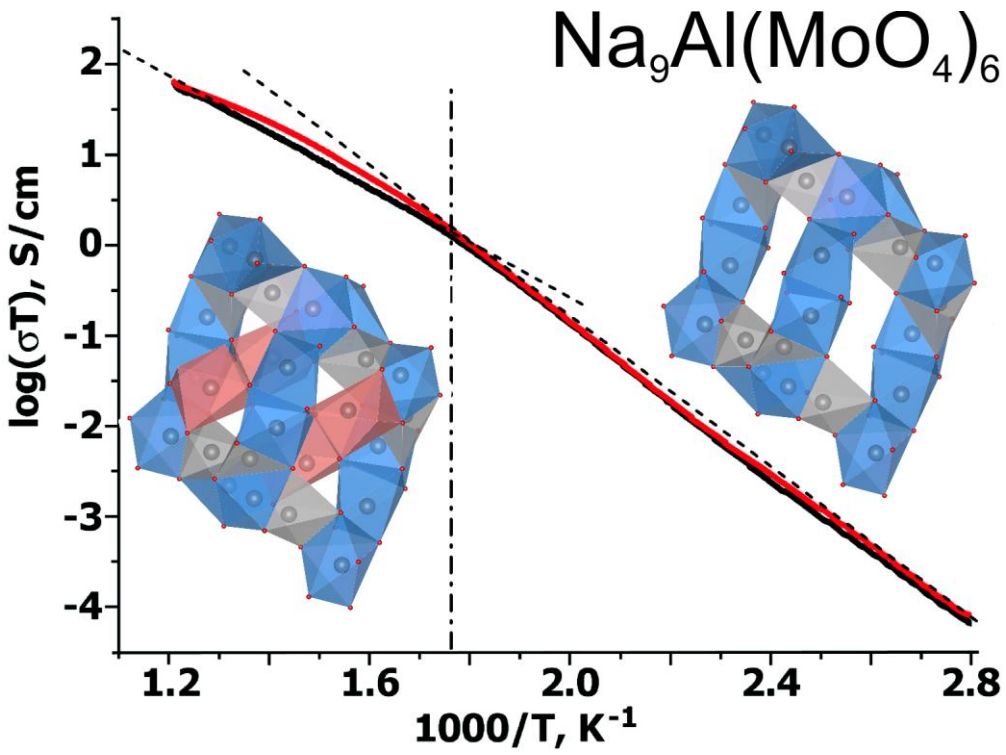

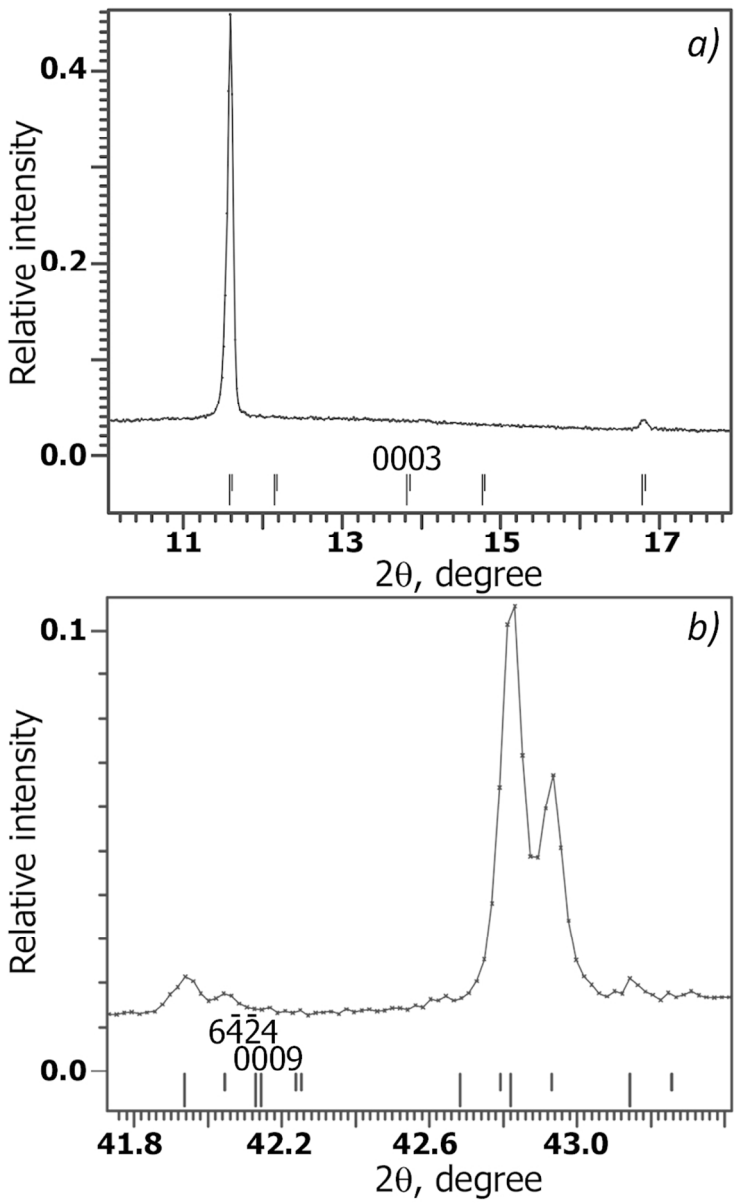

Figure 1. Part of the PXRD patterns of the Na9Al(MoO4)6 in 2θ ranges of 10−18° (a) and 47.7−43.4° (b). Tick marks denote the peak positions and the indexation of possible Bragg reflections.

80x130mm (300 x 300 DPI)

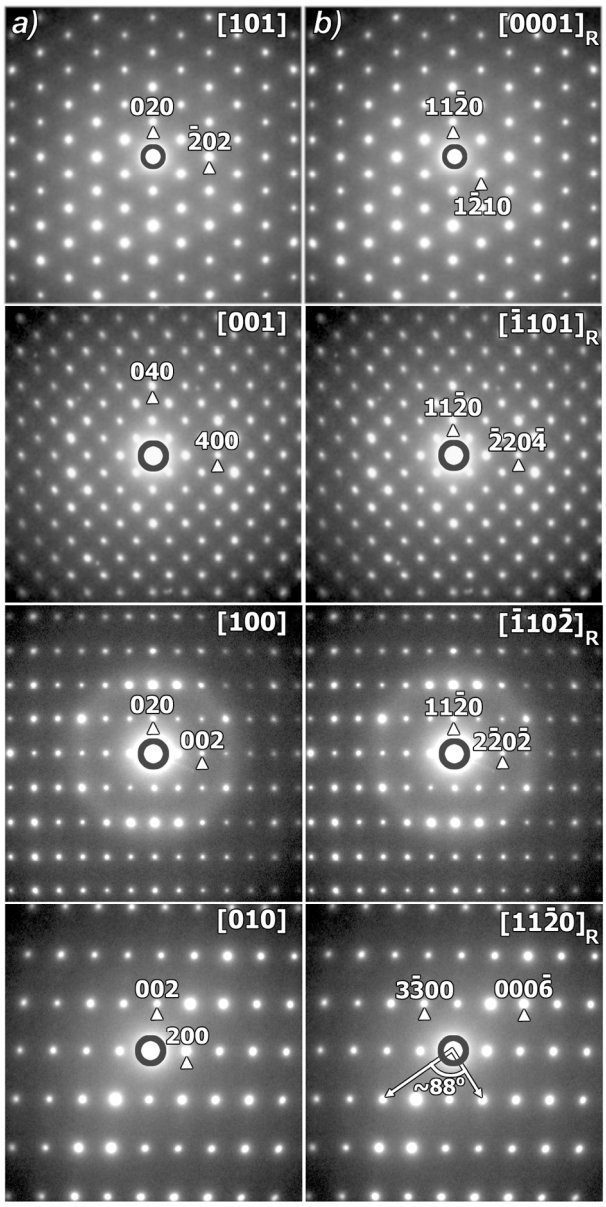

Figure 2. ED patterns along the main zone axes for Na9Al(MoO4)6: a) indexing in the Cc or C2/c space group (left column); b) indexed in the R c space group (right column).

92x184mm (300 x 300 DPI)

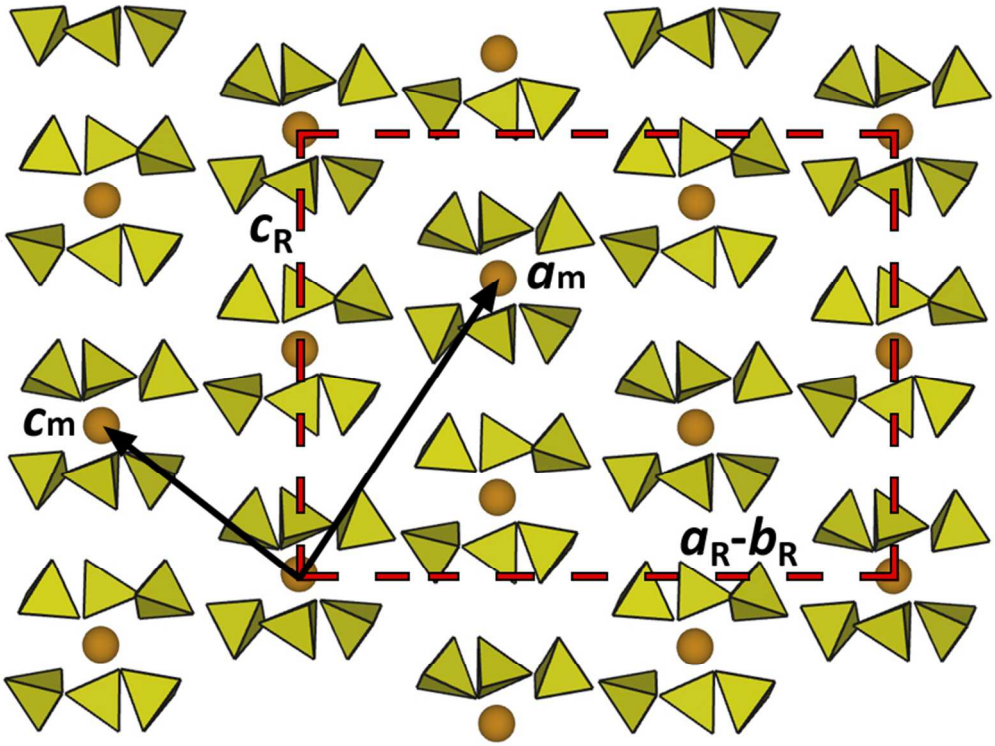

Figure 3. (Color online). Transformation of lattice parameters from R c subcell (marked as aR, bR, cR) to monoclinic C2/c cell (marked as am, cm).

75x57mm (300 x 300 DPI)

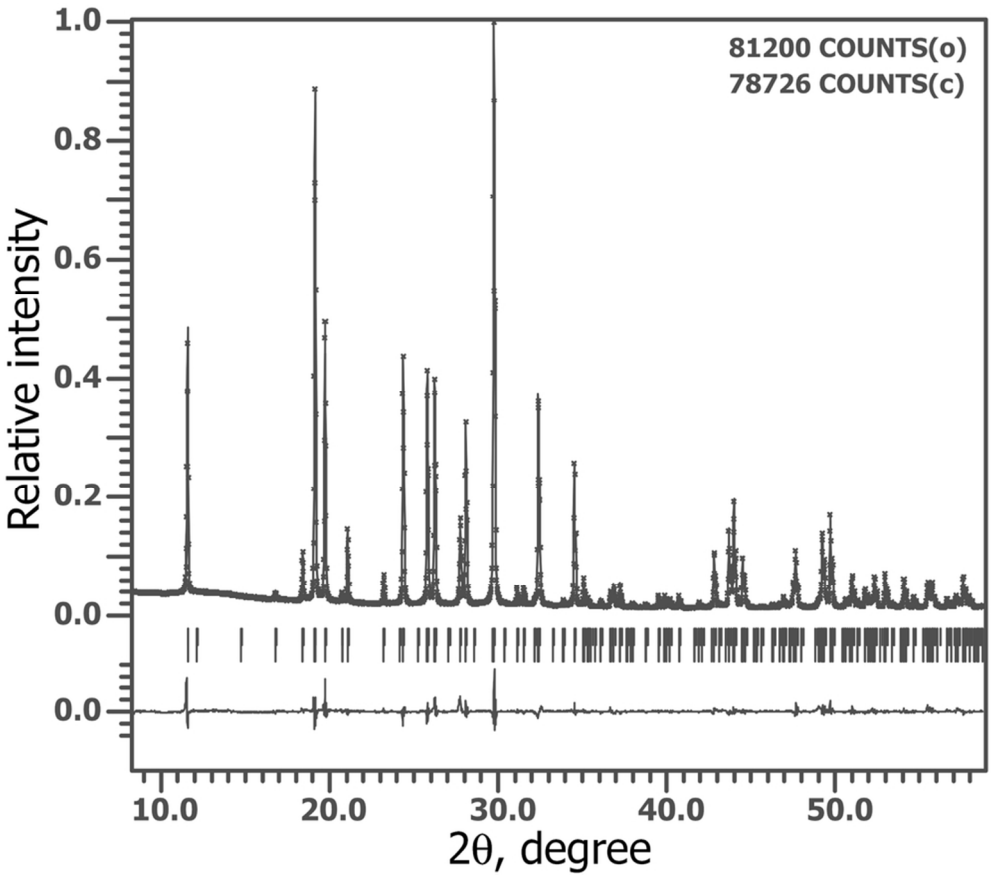

Figure 4. Portions of observed, calculated and difference PXRD patterns for Na9Al(MoO4)6. Tick marks denote the peak positions of possible Bragg reflections.

85x74mm (300 x 300 DPI)

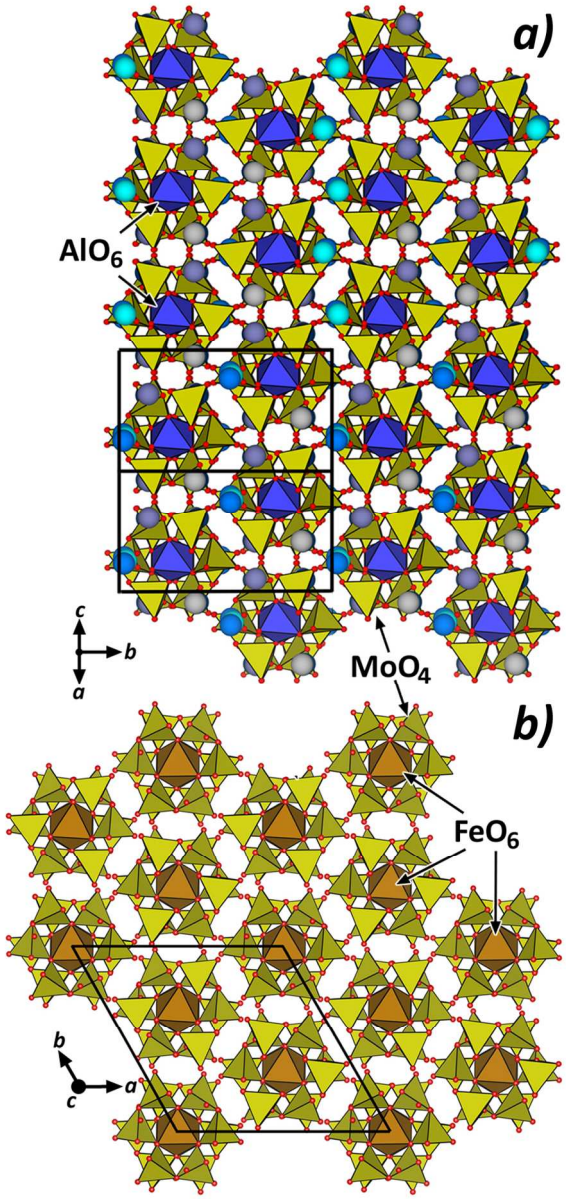

Figure 5. (Color online). Projection of the Na9Al(MoO4)6 structure (a) and a view of the Na9Fe(MoO4)6 structure showing only the [Fe(MoO4)6]9– clusters (b). The large blue spheres and small red spheres indicate Na and oxygen atoms, respectively.

80x166mm (300 x 300 DPI)

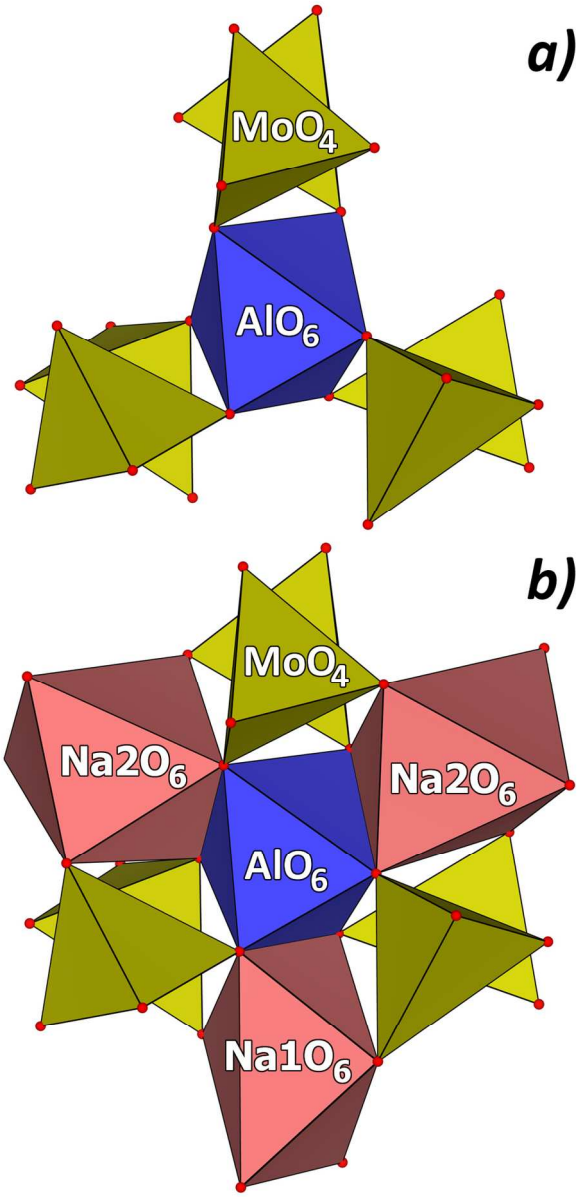

Figure 6. (Color online). [Al(MoO4)6]9– cluster (a) and fragment from [Al(MoO4)6]9– cluster and three NaO6-octahedra in Na9Al(MoO4)6 structure (b).

83x169mm (300 x 300 DPI)

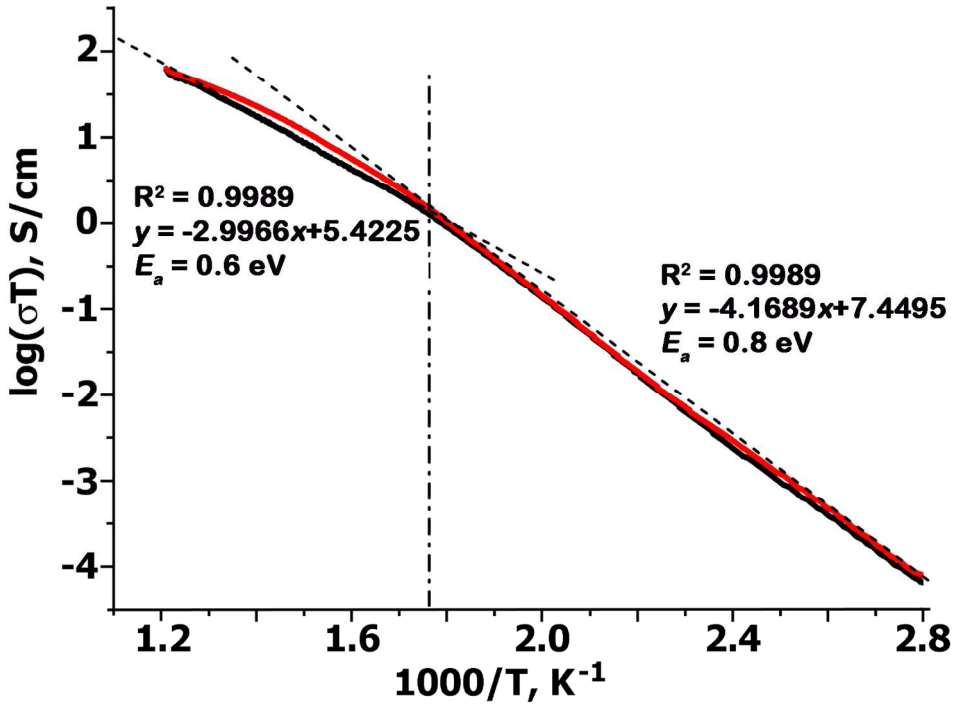

Figure 7. (Color online). Temperature dependence of the conductivity of Na9Al(MoO4)6.

150x110mm (300 x 300 DPI)

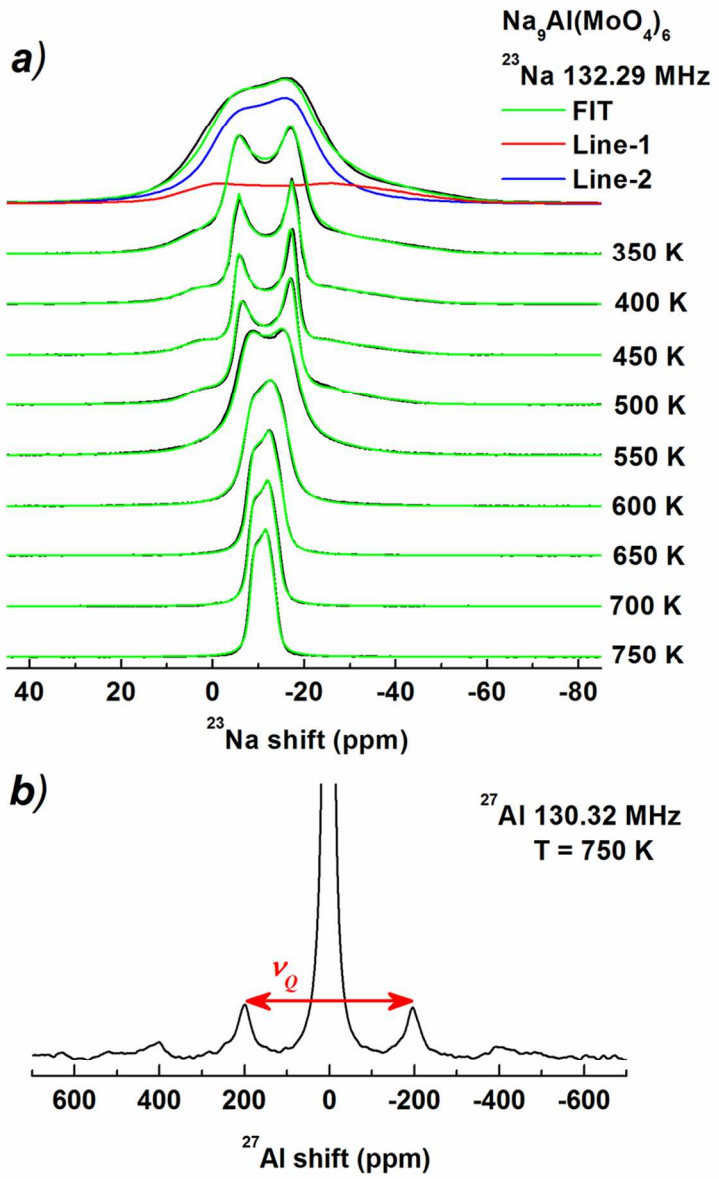

Figure 8. (Color online) (a) The temperature evolution of the 23Na NMR spectrum in Na9Al(MoO4)6 over the temperature range 300–750 K in a magnetic field 11.7 T. Experimental data are shown as black lines, the fitting results by green lines. (b) NMR spectrum of 27Al nuclei measured at 750 K in the field 11.7 T.

80x128mm (300 x 300 DPI)

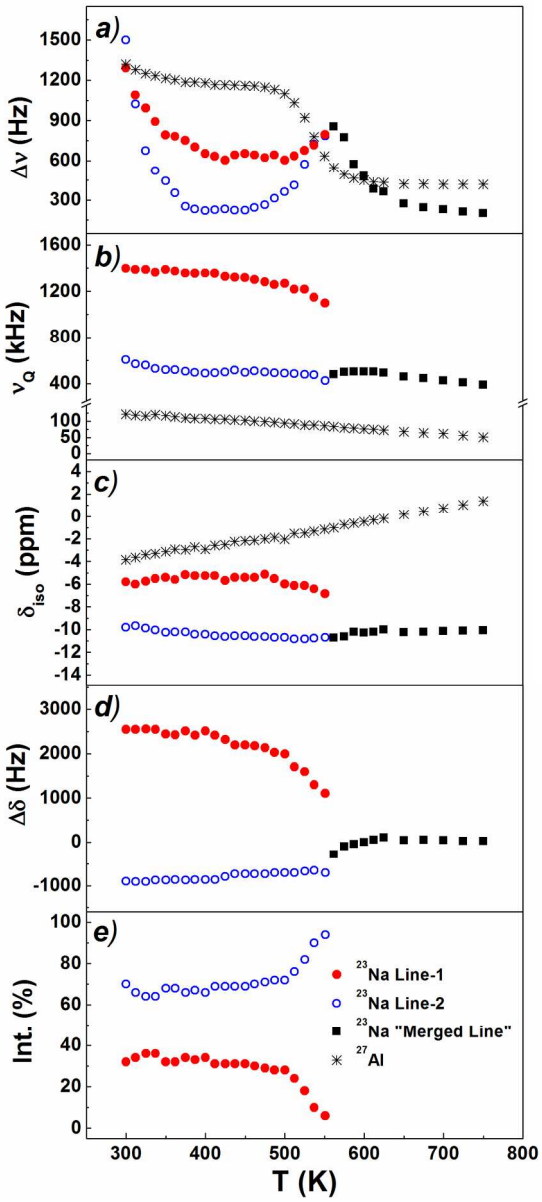

Figure 9. (Color online). Temperature behavior of the 23Na and 27Al NMR signal parameters (11.7 T): (a) central line width, Δν, (b) quadrupole frequency νQ, (c) isotropic shift δiso, (d) chemical shift anisotropy Δδ, and (e) the relative intensities of lines 1 and 2. Filled red and open blue circles correspond to 23Na Line-1 and Line-2, respectively. The black squares correspond to NMR parameters of the signal after the "merging" of lines 1 and 2. Black crosses are the corresponding NMR parameters for 27Al nuclei.

174x378mm (300 x 300 DPI)

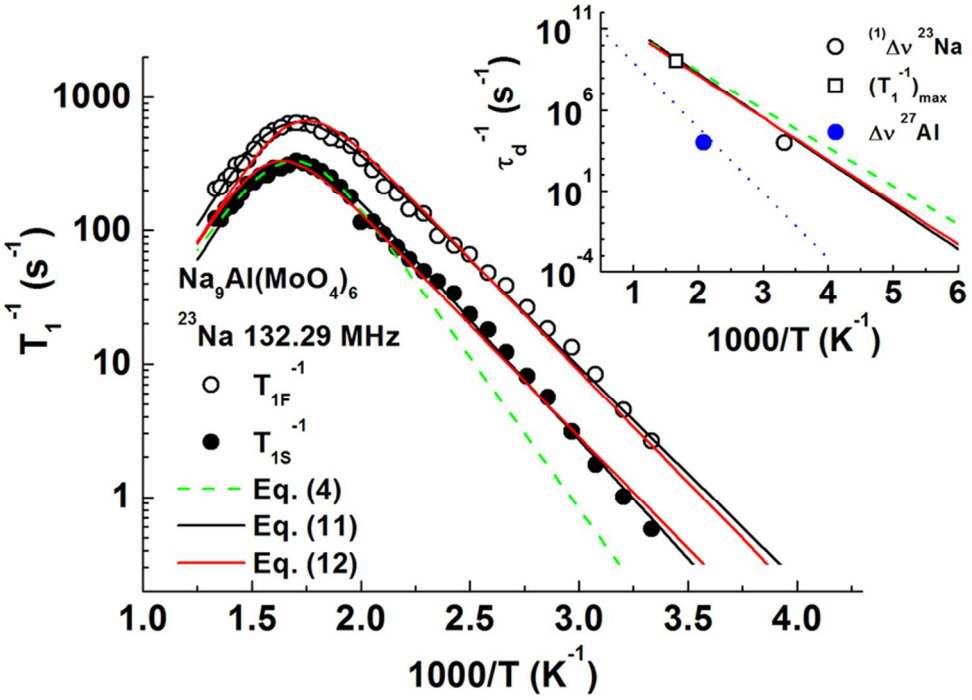

Figure 10. (Color online). Arrhenius plot of the 23Na spin-lattice relaxation rate measured in a magnetic field 11.7 T over the temperature range 300–750 K. The filled and empty circles correspond to the slow (T1S–1) and fast (T1F–1) relaxation components. The green dashed line corresponds to the fit of experimental data on T1S–1 by the BPP model. Black and red solid lines are the approximations of the data on T1S–1 and T1F–1 by the coupling model and generalized coupling model, respectively. The inset shows the estimates of τd-1 for Na+ jumps in the Na(3–5) sites sublattice, the lines correspond to the fit results by BPP model, coupling model and generalized coupling model. The dots – are the estimates of τd-1 obtained from the experimental data on Δν(T) (○) and (T1-1)max (□). The (●) and dotted line are the estimates of τd–1 for Na(1–2) ↔ Na(3–5) jumps, obtained from the analysis of the data on Δν(T) for 27Al and BPP model, respectively.

80x57mm (300 x 300 DPI)

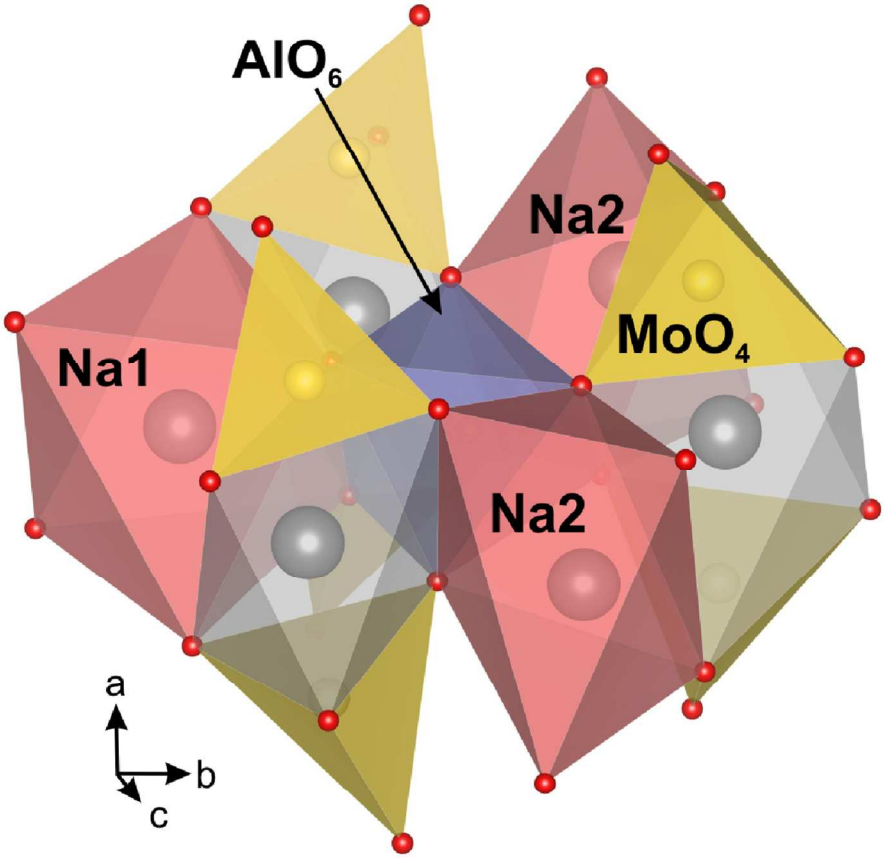

Figure 11. (Color online). Fragment of [Al(MoO4)6]9– cluster with NaO6 octahedra (pale red) and octahedral interstitials (grey) between MoO4 tetrahedra (pale yellow) representing the blocking jumps within the Na1–Na2 sublattice.

120x115mm (300 x 300 DPI)

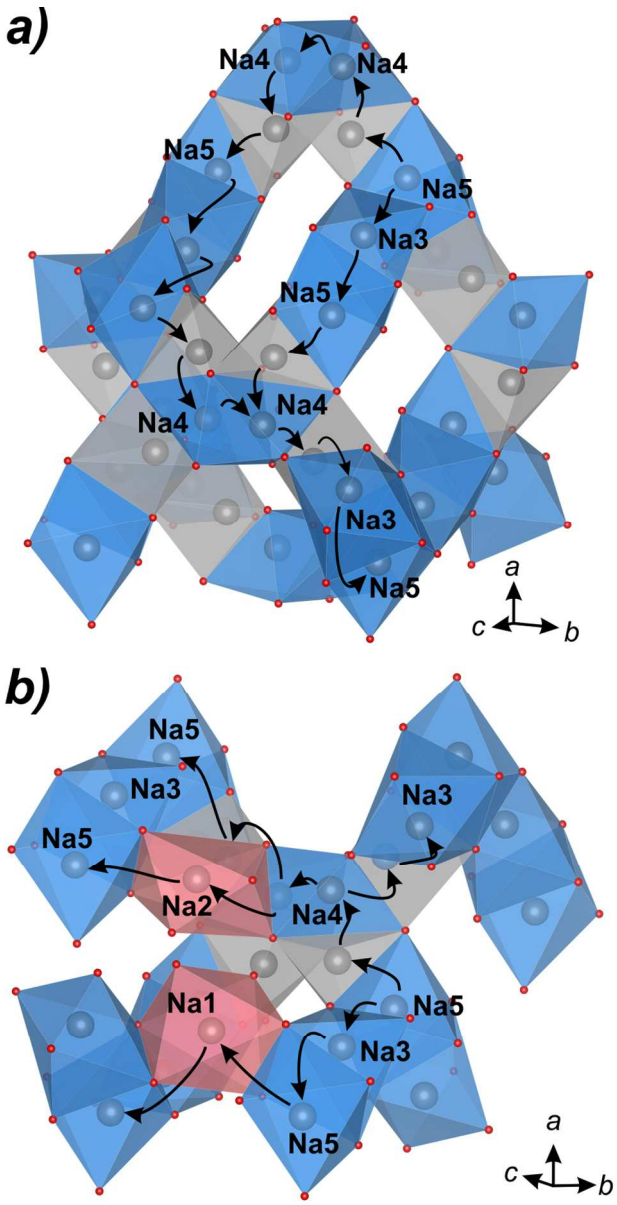

Figure 12. (Color online). The scheme of Na+ transport: a – at temperatures below 490 K exclusively by positions Na3–Na5; b – above 490 K with the involvement of positions Na1–Na2 through the chemical exchange with Na3–Na5 sublattice.

79x153mm (300 x 300 DPI)